

1 **Visibility-derived aerosol optical depth over global land from 1959 to** 2 **2021**

3 Hongfei Hao¹, Kaicun Wang², Chuanfeng Zhao³, Guocan Wu¹, Jing Li³

4 ¹Global Change and Earth System Science, Faculty of Geographical Science, Beijing Normal
5 University, Beijing 100875, China

6 ²Institute of Carbon Neutrality, Sino French Institute of Earth System Science, College Urban and
7 Environmental Sciences, Peking University, Beijing 100871, China

8 ³Institute of Carbon Neutrality, Department of Atmospheric and Oceanic Sciences, School of
9 Physics, College Urban and Environmental Sciences, Peking University, Beijing 100871, China

10 *Corresponding Author: Kaicun Wang (kcwang@pku.edu.cn)*

11 **Abstract**

12 Long-term and high spatial resolution aerosol optical depth (AOD) data are essential for climate
13 change detection and attribution. Global ground-based AOD observations are sparsely distributed,
14 and satellite AOD retrievals have a low temporal frequency, as well low accuracy before 2000 over
15 land. In this study, AOD at 550nm is derived from visibility observations collected at more than
16 5000 meteorological stations over global land from 1959 to 2021. The AOD retrievals (550nm) of
17 the Moderate Resolution Imaging Spectroradiometer (MODIS) onboard the Aqua Earth observation
18 satellite are used to train the machine learning model, and the ERA5 reanalysis boundary layer
19 height is used to convert the surface visibility to AOD. Comparison with independent dataset
20 (AERONET ground-based observations) shows that the predicted AOD has a correlation coefficient
21 of 0.55 at daily scale. The correlation coefficients are higher at monthly and annual scales, which
22 are 0.61 for the monthly and 0.65 for the annual, respectively. The evaluation result shows consistent
23 predictive ability prior to 2000, with a correlation coefficient of 0.54, 0.66 and 0.66 at daily, monthly,
24 and annual scales, respectively. Due to a small number and sparse visibility stations prior to 1980,
25 the global/regional analysis in this study is from 1980 to 2021. From 1980 to 2021, the mean
26 visibility-derived AOD over the global land, the Northern Hemisphere, and the Southern
27 Hemisphere are 0.177, 0.178, and 0.175, with a trend of -0.0029/10a, -0.0030/10a, and -0.0021/10a
28 from 1980 to 2021. The regional mean trends of AOD are 0.181 (-0.0096/10a), 0.163 (-0.0026/10a),
29 0.146 (-0.0017/10a), 0.165 (-0.0027/10a), 0.198 (-0.0075/10a), 0.281 (-0.0062/10a), 0.182 (-
30 0.0016/10a), 0.133 (-0.0028/10a), 0.222 (0.0007/10a), 0.244 (-0.0009/10a), 0.241 (0.0130 /10a),
31 and 0.254 (0.0119/10a) in Eastern Europe, Western Europe, Western North America, Eastern North
32 America, Central South America, Western Africa, Southern Africa, Australia, Southeast Asia,
33 Northeast Asia, Eastern China, and India, respectively. However, the trends are decreasing
34 significantly in Eastern China (-0.0572/10a) and Northeast Asia (-0.0213/10a) after 2014 and the
35 larger increasing trend is found after 2005 in India (0.0446/10a). The visibility-derived daily AOD
36 dataset at 5032 stations over global land from 1959 to 2021 are available at National Tibetan Plateau
37 / Third Pole Environment Data Center (<https://doi.org/10.11888/Atmos.tpd.300822>) (Hao et al.,

38 2023).
39 How to cite. Hao, H., Wang, K., C. Zhao, Wu, G., J. Li (2023). Visibility-derived aerosol optical
40 depth over global land (1959-2021). National Tibetan Plateau / Third Pole Environment Data
41 Center. <https://doi.org/10.11888/Atmos.tpdc.300822>.

42 **1 Introduction**

43 Atmospheric aerosols are composed of solid and liquid particles suspended in the atmosphere.
44 Aerosol particles are directly emitted into the atmosphere or formed through gas-particle
45 transformation (Calvo et al., 2013), with diverse shapes and sizes (Fan et al., 2021), optical
46 properties, and components (Liao et al., 2015; Zhang et al., 2020; Li et al., 2022). Most atmospheric
47 aerosols are concentrated in the troposphere, especially in the boundary layer (Liu et al., 2022), with
48 a high concentration near emission sources (Kulmala et al., 2004) , and a small portion are
49 distributed in the stratosphere. Atmospheric aerosols severely impact the atmospheric environment
50 and human health. They deteriorate air quality, reduce visibility, and cause other environmental
51 issues (Wang et al., 2012; Boers et al., 2015). They impair human health or other organisms'
52 conditions by increasing cardiovascular and respiratory disease incidence and mortality rates (Chafe
53 et al., 2014; Yang et al., 2022). The Global Burden of Disease shows that global exposure to ambient
54 PM_{2.5} (particulate matter suspended in air with an aerodynamic diameter of less than 2.5
55 micrometers) resulted in 0.37 million deaths and 9.9 million disability-adjusted life years (Chafe et
56 al., 2014).

57 Aerosols are inextricably linked to climate change. Atmospheric aerosols alter the Earth's energy
58 budget and affect the climate (Li et al., 2022). They cool the surface and heat the atmosphere by
59 scattering and absorbing solar radiation (Forster et al., 2007; Chen et al., 2022). Aerosols, such as
60 black carbon and brown carbon, also absorb solar radiation (Bergstrom et al., 2007), heat the local
61 atmosphere and suppress or invigorate convective activities (Ramanathan et al., 2001; Sun and Zhao,
62 2020). Aerosols also alter the optical properties and life span of clouds (Albrecht, 1989).
63 Atmospheric aerosols strongly affect regional and global short-term and long-term climates through
64 direct and indirect effects (Mcneill, 2017).

65 Tropospheric aerosols are considered as the second largest forcing factor for global climate change
66 (Li et al., 2022), and they reduce the warming due to greenhouse gases by -0.5°C (IPCC, 2021).
67 However, aerosols are also regarded as the largest contributor to the uncertainty of present-day
68 climate change attribution (IPCC, 2021). The uncertainties are caused by the deficiencies of the
69 global descriptions of aerosol optical properties (such as scattering and absorption) and
70 microphysical properties (such as size and component), and the impact on cloud and precipitation,
71 further affecting the estimation of aerosol radiative forcing (Lee et al., 2016; IPCC, 2021). Therefore,
72 sufficient aerosol observations are crucial. In aerosol measurements, aerosol optical depth (AOD)
73 is often used to describe its column properties, which represents the vertical integration of aerosol
74 extinction coefficients. AOD is an important physical quantity for estimating the content,
75 atmospheric pollution and climatology of aerosols (Zhang et al., 2020).

76 AOD data usually from ground-based and satellite-borne remote sensing observations. They have
77 both advantages and disadvantages. Ground-based lidar observation is an active remote sensing

78 technology. Lidar generally emits laser and receives backscattered signals to invert the extinction
79 coefficient of aerosols at different heights (Klett, 1985). By using the depolarization ratio, the type
80 of aerosol, such as fine particles or dust, can be distinguished (Bescond et al., 2013). The AOD
81 within a certain height can be calculated by integrating the extinction coefficients; however,
82 scattering signals are usually not received near the ground, leading to blind spots (Singh et al., 2019).
83 At present, there are many ground-based lidar worldwide and regional networks, which provides
84 important support of vertical changes in aerosols, such as the NASA Micro-Pulse Lidar Network
85 (MPLNET) in the early 1990s (Welton et al., 2002), the European Aerosol Research Lidar Network
86 (EARLINET) since 2000 (Bösenberg and Matthias, 2003), the Latin American Lidar Network
87 (LALINET) since 2013 (Guerrero-Rascado et al., 2016).

88 Ground-based remote sensing observations supply aerosol loading data (such as AOD), by
89 measuring the attenuation of radiation from the top of the atmosphere to the surface (Holben et al.,
90 1998). This type of observation mainly uses weather-resistant automatic sun and sky scanning
91 spectral radiometers to retrieve optical and microphysical aerosol properties (Che et al., 2014). The
92 Aerosol Robotic Network (AERONET) is a popular global network composed of NASA and
93 multiple international partners that provides high-quality and high-frequency aerosol optical and
94 microphysical properties under various geographical and environmental conditions (Holben et al.,
95 1998; Dubovik et al., 2000). The AERONET observations are extensively used to validate satellite
96 remote sensing observations and model simulations, as well as climatology study (Dubovik et al.,
97 2002b). There are many regional networks of sun photometers, such as the Maritime Aerosol
98 Network (MAN), which use a handheld sun photometer to collect data over the ocean and is merged
99 into AERONET (Smirnov et al., 2009), the China Aerosol Robot Sun Photometer Network
100 (CARSNET) (Che et al., 2009), the Canadian sub-network of AERONET (AEROCAN) (Bokoye et
101 al., 2001), Aerosol characterization via Sun photometry: Australian Network (AeroSpan)
102 (Mukkavilli et al., 2019), and the sky radiometer network (SKYNET) in Asia and Europe (Kim et
103 al., 2004; Nakajima et al., 2020). Another very valuable global network is the NOAA/ESRL
104 Federated Aerosol Network (FAN), which uses integrated nephelometers distinct from sun
105 photometers, mainly located in remote areas, providing background aerosol properties over 30 sites
106 (Andrews et al., 2019).

107 Satellite remote-sensing is a space-based method that can provide aerosol properties worldwide.
108 With the development of satellite remote sensing technology since 1970s, aerosol distributions can
109 be extracted with the advantage of sufficient real-time and global coverage from multiple satellite
110 sensors (Kaufman and Boucher, 2002; Anderson et al., 2005). The Advanced Very High Resolution
111 Radiometer (AVHRR) is the earliest sensor used for retrieving AOD over ocean (Nagaraja Rao et
112 al., 1989). The Moderate Resolution Imaging Spectroradiometer (MODIS), on board the Terra
113 (launched in 1999) and Aqua (launched in 2002) satellites is a popular sensor with 36 channels,
114 which have been used for AOD retrieval over both ocean and land based on the Dark Target and the
115 Deep Blue algorithms (Remer et al., 2005; Levy et al., 2013). The latest MODIS AOD data version
116 is the Collection 6.1, which provides global AOD over 20 years (Wei et al., 2019). There are also
117 many other satellite sensors that can be used to retrieve AOD, such as the Polarization and
118 Directionality of the Earth's Reflectances (POLDER) during 1996-1997, 2003 and 2004-2013
119 (Deuzé et al., 2000), Sea-viewing Wide Field-of-view Sensor (SeaWiFS) during 1997-2007
120 (O'reilly et al., 1998), the Multi-angle Imaging Spectroradiometer (MISR) on Terra since 1999

121 (Diner et al., 1998). The Cloud-Aerosol Lidar with Orthogonal Polarization (CALIOP) has also
122 derived aerosols in the vertical direction since 2006 (Winker et al., 2009).

123 These measurements provide important data for studying the global and regional spatiotemporal
124 variabilities and climate effect of aerosols. However, ground-based remote sensing observations
125 only provide aerosol properties with low spatial coverage. There were only about 150 ground
126 stations worldwide in 2002 and even fewer sites were available for climate analysis (Holben et al.,
127 1998; Chu et al., 2002), which limited aerosol climate research by spatial coverage (Bright and
128 Gueymard, 2019). Satellite remote sensing overcomes the limitations of spatial coverage. The
129 AVHRR has been used to retrieve AOD since 1980, but it is limited by a few channel number, low
130 spatial resolution, and insufficient validation through ground-based observations before 2000 (Hsu
131 et al., 2017). Many studies have only investigated the trends and distributions of aerosols after 2000
132 (Bösenberg and Matthias, 2003; Winker et al., 2013; Xia et al., 2016; Tian et al., 2023), because of
133 the lack of long-term and global cover AOD products, which is the bottleneck for aerosol climate
134 change detection and attributions.

135 To overcome these limitations and enrich aerosol data, alternative observation data could be utilized
136 to derive AOD. Atmospheric horizontal visibility is a suitable alternative (Wang et al., 2009; Zhang
137 et al., 2020), because it has the advantages of the long-term records with a large number of stations
138 worldwide.

139 Atmospheric visibility is a physical quantity that describes the transparency of the atmosphere
140 through manual and automatic observations, and the automatic observations of visibility usually
141 measure atmospheric extinction (scattering coefficient and transmissivity). Koschmieder (1924)
142 first proposed the relationship between the meteorological optical range and the total optical depth.
143 Elterman (1970) further established a formula between AOD and visibility by assuming an
144 exponential decrease in aerosol concentration with altitude, considering the extinction of molecules
145 and ozone to analyze air pollution, which called the Elterman model. Qiu and Lin (2001) corrected
146 the Elterman model by considering the influence of water vapor and used two water vapor pressure
147 correction coefficients to retrieve AOD of 16 stations in China in 1990. Wang et al. (2009) analyzed
148 the trend of AOD using visibility-based retrievals from 1973 to 2007 over land. Lin et al. (2014)
149 retrieved the AOD in eastern China in 2006 using visibility and aerosol vertical profiles provided
150 by GEOS-Chem. Wu et al. (2014) and Zhang et al. (2017) parameterized the constants in the
151 Elterman model and use satellite retrieved AOD to solve the parameters in the models at different
152 stations, to retrieve the long-term AOD in China.

153 Zhang et al. (2020) reviewed the methods of visibility retrieval of AOD, indicating that visibility-
154 based retrieval of AOD can compensate for the shortcomings of long-term aerosol observation data.
155 Simultaneously, various parameters, such as station altitude, consistency of visibility data, water
156 vapor and aerosol vertical profiles (scale height), were discussed with modified suggestions
157 proposed. These studies have enriched AOD data regionally. These studies have enriched aerosol
158 data in some extent. At present, there are very few studies on global visibility-retrieved AOD and to
159 analyze climatology of aerosols.

160 The two physical quantities of visibility and AOD have both connections and differences, making it
161 challenging to retrieve AOD from visibility. Visibility represents the maximum horizontal visible
162 distance near the surface, while AOD represents the total vertical attenuation of solar radiation by

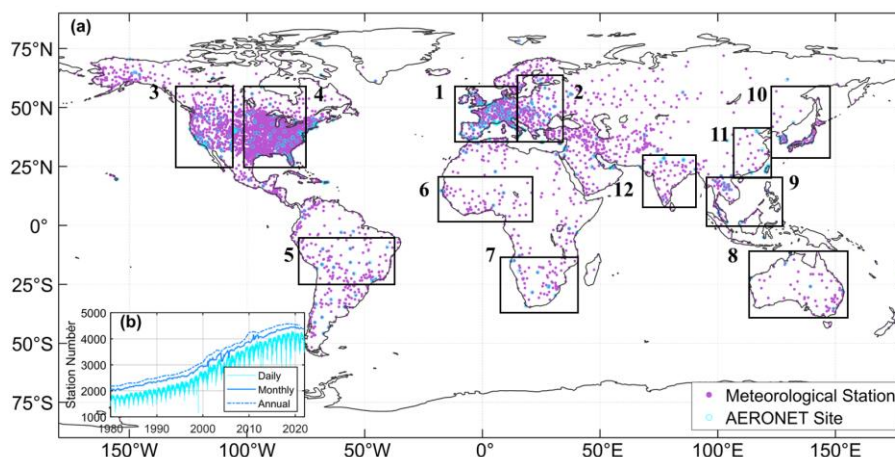
163 aerosols. The visibility of automatic observation is dependent on the local horizontal atmospheric
164 extinction (Noaa et al., 1998). Visibility has not a simple linear relationship with meteorological
165 factors. The vertical structure of aerosols is the greatest challenge to obtain, as it is not a simple
166 hypothetical curve in complex terrain and circulation conditions (Zhang et al., 2020). These
167 limitations make it more complex to derive AOD. Machine learning methods can effectively address
168 complex nonlinear relationships between variables and have been widely applied in remote sensing
169 and climate research fields. Li et al. (2021) used the random forest method to predict PM_{2.5} in Iraq
170 and Kuwait based on satellite AOD during 2001-2018. Kang et al. (2022) applied LightGBM and
171 random forest to estimate AOD over East Asia, and the results showed a consistency with
172 AERONET. Dong et al. (2023) derived aerosol single scattering albedo from visibility and satellite
173 AOD over 1000 global stations. Hu et al. (2019) used a deep learning method to retrieve horizontal
174 visibility from MODIS AOD. These studies have confirmed the ability of machine learning to
175 effectively solve complex relationships among variables. Previous studies are mostly conducted at
176 the regional or national scale, and few studies at the global scale. Thus, it is feasible to derive AOD
177 from atmospheric visibility over global land by using the machine learning method.

178 In this study, we propose a machine learning method to derive AOD, where satellite AOD is the
179 target value, and visibility and other related meteorological variables are the predictors. We explain
180 the model's robustness, and evaluate the model's predictive ability, and validate the model's
181 predictions using independent ground-based AOD, satellite retrievals and reanalysis AOD, and
182 analyze the mean and trend of AOD across land and regions. A station-scale dataset of long-term
183 AOD is generated. The Section 2 introduces the data and method. The Section 3 is the evaluation
184 and validation of the visibility-derived AOD, and the distribution and trends are discussed at global
185 and regional scales. The Section 5 presents the conclusions. This study is dedicated to supporting
186 the research of aerosols in climate change detection and attribution.

187 **2 Data and method**

188 **2.1 Study area**

189 The study area is global land. A total of 5032 meteorological stations and 395 AERONET sites are
190 selected in this study, shown in Figure 1. Twelve regions are selected for special analysis, including
191 Eastern Europe, Western Europe, Western North America, Eastern North America, Central South
192 America, Western Africa, Southern Africa, Australia, Southeast Asia, Northeast Asia, Eastern China,
193 and India and the station number is 187, 494, 390, 1759, 132, 72, 78, 86, 76, 140, 26, and 51,
194 respectively. The meteorological observations data including visibility are available since 1959. The
195 time range of global and regional average analysis is from 1980 to 2021, during which the visibility
196 observations are sufficient with a uniform spatial distribution. As shown in Figure 1, the daily
197 visibility records have exceeded 1100 stations, and monthly and annual records have exceeded 2000
198 during 1980-1990. After 2000, monthly records have reached 3000.



199

200 **Figure 1:** Study area (a) and the meteorological station number (b) at daily, monthly, and annual
 201 scale. The number of meteorological stations (filled circles) is 5032. The number of AERONET
 202 sites (empty circles) is 395. The box regions of labelled with number 1-12 are Eastern Europe,
 203 Western Europe, Western North America, Eastern North America, Central South America, Western
 204 Africa, Southern Africa, Australia, Southeast Asia, Northeast Asia, Eastern China, and India.

205 **2.2 Meteorological data**

206 The hourly ground-based meteorological data from 1959 to 2021 is collected from 5032
 207 meteorological stations of airports over land, which can be downloaded at
 208 <https://mesonet.agron.iastate.edu/ASOS>. Over 1000 stations belong to the Automated Surface
 209 Observing System (ASOS), and others are sourced from airport reports around the world. The
 210 visibility measurements can be divided into automatic observation and manual observation.
 211 Automatic visibility observations reduce errors associated with human involvement in data
 212 collection, processing, and transmission. The visibility and other meteorological data are extracted
 213 from the Meteorological Terminal Aviation Routine Weather Report (METAR). The World
 214 Meteorological Organization (WMO) sets guidelines for METAR reports, including report format,
 215 encoding, observation instruments and methods, data accuracy, and consistency, which ensures the
 216 consistency and comparability of METAR reports globally. Some international regulations can be
 217 referenced at [https://community.wmo.int/en/implementation-areas-aeronautical-meteorology-](https://community.wmo.int/en/implementation-areas-aeronautical-meteorology-programme)
 218 [programme](https://community.wmo.int/en/implementation-areas-aeronautical-meteorology-programme).

219 The daily average visibility is calculated using harmonic mean in equation (1). The reciprocal of
 220 visibility is proportional to the extinction coefficient (Wang et al., 2009). Experiments have found
 221 that harmonic average visibility can better detect the weather phenomena than arithmetic average
 222 visibility, when visibility decline quickly (Noaa et al., 1998). Therefore, daily visibility will have
 223 greater representativeness.

224 In addition to hourly visibility (VIS), other variables closely related to aerosol properties are selected,
 225 including relative humidity (RH), dew point temperature (DT), temperature (TMP), wind speed
 226 (WS) and sea-level pressure (SLP). Because air temperature affects atmospheric stability and the
 227 rate of secondary particle formation, and humidity influences the size and hygroscopic growth, and
 228 wind speed and pressure significantly impact the transport and deposition. Sky conditions (cloud

229 amount) and hourly precipitation are also selected to remove the records of extensive cloud cover
230 and precipitation.

231 We processed the meteorological data as follows. The records with high missing value ratio are
232 eliminated (Husar et al., 2000). When over 80% overcast or fog, the records of sky conditions are
233 eliminated, though such situations occur less than 1% of the time over land (Remer et al., 2008).
234 The records with 1-hour precipitation greater than 0.1 mm are eliminated. We calculate the
235 temperature dew point difference (dT). The low visibility records under “blowing snow” weather
236 are eliminated at high latitude region ($> 65^{\circ}\text{N}$), when wind speed is great than 4.5m/s (Husar et al.,
237 2000). When the RH is greater than 90%, it is impossible to distinguish whether it is fog or haze, or
238 both, and even precipitation. Therefore, the records with RH greater than or equal to 90% are
239 eliminated. When the RH is less than 30%, the hygroscopic effect of aerosols is very low or even
240 negligible. When RH is between 30% and 90%, the hygroscopic effect of aerosols is high, and
241 visibility is converted to dry visibility (Yang et al., 2021c), as shown in equation (2). At least 3
242 hourly records of meteorological variables are required when calculating the daily average ($n \geq 3$).

$$243 \quad V = n / \left(\frac{1}{V_1} + \frac{1}{V_2} + \dots + \frac{1}{V_n} \right), \quad (1)$$

244 where V is the harmonic mean visibility, n is the daily record number, and V_1, V_2, \dots, V_n are the
245 individual hourly visibility.

$$246 \quad VISD = VIS / (0.26 + 0.4285 * \log(100 - RH)), \quad (2)$$

247 where $VISD$ is the dry visibility.

248 **2.3 Boundary layer height**

249 The hourly boundary layer height (BLH) data from 1980 to 2021 are available from the Fifth
250 Generation reanalysis of the European Medium-Range Weather Forecast Center (ERA5) with a
251 resolution of $0.25^{\circ} \times 0.25^{\circ}$ (<https://cds.climate.copernicus.eu>), which is the successor of ERA-
252 Interim and has undergone various improvements (Hersbach et al., 2020). The atmospheric
253 boundary layer is the layer closest to the Earth’s surface and exhibits complex turbulence activities,
254 and its height undergoes significant diurnal variation. The boundary layer play a crucial role in
255 regulating and adjusting the distribution of atmospheric aerosols, such as vertical distribution,
256 concentration changes, transport, and deposition (Ackerman et al., 1995). The boundary layer height
257 serves as an approximate measure of the scale height for aerosols (Zhang et al., 2020).

258 Compared to observations of 300 stations over world from 2012 to 2019, the ERA5 BLH is
259 underestimated by 131.96m, and it is closest to the observations compared to JRA-55, and NECP-
260 2 BLH (Guo et al., 2021). The hourly BLH data is temporally and spatially matched with visibility
261 and other meteorological data before calculating the daily average.

262 Because the reciprocal of visibility is proportional to the extinction coefficient and positively related
263 to AOD (Wang et al., 2009), we calculate the reciprocal of visibility (VISI) and the reciprocal of dry
264 visibility (VISDI). Due to the influence of boundary layer height on the vertical distribution of
265 particles (Zhang et al., 2020), we calculate the product (VISDIB) of VISDI and BLH. Therefore,
266 the Predictor (Figure 2) is composed of 11 variables (TMP, Td, dT, RH, SLP, WS, VIS, BLH, VISI,
267 VISDI, and VISDIB).

268 **2.4 MODIS AOD products**

269 Satellite daily AOD is available from the Moderate Resolution Imaging Spectroradiometer (MODIS)
270 Level 3 Collection 6.1 AOD products of the Aqua (MYD09CMA) satellite from 2002 to 2021 and
271 Terra (MOD09CMA) satellite from 2000 to 2021 with a spatial resolution of $0.05^\circ \times 0.05^\circ$ at a
272 wavelength of 550 nm (<https://ladsweb.modaps.eosdis.nasa.gov>). Terra (passing 10:30 am at local
273 time) and Aqua (passing 1:30 pm at local time) are successfully launched in December 1999 and
274 May 2002, respectively. MODIS, carried on the Terra and Aqua satellites is a crucial instrument in
275 the NASA Earth Observing System program, which is designed to observe global biophysical
276 processes (Salomonson et al., 1987). The 2330 km-wide swath of the orbit scan can cover the entire
277 globe every one to two days. MODIS has 36 channels and more spectral channels than previous
278 satellite sensors (such as AVHRR). The spectrum ranges from 0.41 to $15\mu\text{m}$ representing three
279 spatial resolutions: 250 m (2 channels), 500 m (5 channels), and 1 km (29 channels). The aerosol
280 retrievals use seven of these channels ($0.47\text{--}2.13\mu\text{m}$) to retrieve aerosol characteristics and use
281 additional wavelengths in other parts of the spectrum to identify clouds and river sediments.
282 Therefore, it has the ability to characterize the spatial and temporal characteristics of the global
283 aerosol field.

284 The MODIS aerosol product actually uses different algorithms to retrieve aerosols over land and
285 ocean. The Dark Target (DT) algorithm is applied to densely vegetated areas because the surface
286 reflectance over dark-target areas is lower in the visible channels and has nearly fixed ratios with
287 the surface reflectance in the shortwave and infrared channels (Levy et al., 2007; Levy et al., 2013).
288 The Deep Blue (DB) algorithm is originally applied to bright land surfaces (such as deserts), and
289 later extended to cover all cloud-free and snow-free land surfaces (Hsu et al., 2006; Hsu et al., 2013).
290 MODIS Collection 6.1 aerosol product is released in 2017, incorporating significant improvements
291 in radiometric calibration and aerosol retrieval algorithms.

292 The aerosol retrievals usually are evaluated by the expected error. For the DT algorithm, the
293 expected error is $\pm(0.05\pm 15\% \text{AOD}_{\text{AERONET}})$. The coverage of retrieval products varies by season
294 based on the DT algorithm over land. Higher spatial coverage is observed in August and September,
295 reaching 86-88%. During December and January, due to the presence of permanent ice and snow
296 cover in high-latitude regions of the Northern Hemisphere, the spatial coverage is 78-80%. Thus,
297 challenges remain in retrieving AOD values in high-latitude regions (Wei et al., 2019). However,
298 visibility observations are available in high-latitude regions, thereby partially addressing the lack in
299 these regions. In this study, the Terra and Aqua MODIS AOD are temporally and spatially matched
300 with the meteorological stations. Aqua MODIS AOD is used as the Target when training the model,
301 and Terra MODIS AOD is used in the evaluation and validation of the model results, as shown in
302 the flowchart (Figure 2).

303 **2.5 Ground-based AOD**

304 Ground-based 15-minute AOD observations are available from the Aerosol Robotic Network
305 (AERONET) Version 3.0 Level 2.0 product at 395 sites (Figure 1), which can be downloaded from
306 <https://aeronet.gsfc.nasa.gov>. The AERONET program is a federation of ground-based remote
307 sensing aerosol networks established by NASA and PHOTONS, including many subnetworks (such
308 as AeroSpan, AEROCAN, NEON, and CARSNET). The sun photometer (CE-318) measures
309 spectral sun and sky irradiance in the 340-1020 nm spectral range. AERONET has three levels of
310 AOD products: Level 1.0 (unscreened), Level 1.5 (cloud screened), and Level 2.0 (cloud screened

311 and quality assured). Compared to Version 2, the Version 3 Level 2.0 database has undergone further
312 cloud screening and quality assurance, which is generated based on Level 1.5 data with pre- and
313 post-calibration and temperature adjustment and is recommended for formal scientific research
314 (Giles et al., 2019). AERONET provides AOD products at wavelengths of 440, 675, 870, and 1020
315 nm. When the aerosol loading is low, the error is significant. When the AOD at 440 nm wavelength
316 is less than 0.2, the error is 0.01, which is equivalent to the error of the absorption band in the total
317 optical depth (Dubovik et al., 2002a). The total uncertainty in AOD under cloud-free conditions is
318 less than ± 0.01 , when the wavelength is more than 440 nm, and ± 0.02 when the wavelength is less
319 than 440 nm (Holben et al., 1998). AERONET AOD is usually considered as the ‘true’ value. The
320 AOD at 440nm and the Ångström index at 440-675nm are used to calculate AOD at 550 nm (not
321 provided by AERONET), as shown in equation (3).

$$322 \quad \tau_{550} = \tau_{440} \left(\frac{550}{440} \right)^{-\alpha}, \quad (3)$$

323 where τ_{440} and τ_{550} are the AOD at a wavelength of 440nm and 550 nm, and α is the Ångström
324 index.

325 The daily average AOD requires at least two observations within 1 hour (± 30 minutes) of
326 Aqua/Terra transit time (Wei et al., 2019). The matching conditions between AERONET sites and
327 meteorological stations are (1) a distance of less than 0.5 °, and (2) at least three years of
328 observations. Finally, a total of 395 sites are selected.

329 **2.6 AOD reanalysis dataset**

330 The monthly AOD (550nm) dataset of Modern-Era Retrospective Analysis for Research and
331 Applications version 2 (MERRA-2) from 1980 to 2021 is a NASA reanalysis of the modern satellite
332 era produced by NASA’s Global Modeling and Assimilation Office with a spatial resolution of
333 $0.5 \times 0.625^\circ$ (Gelaro et al., 2017), available at <https://disc.gsfc.nasa.gov>. MERRA-2 AOD uses an
334 analysis splitting technique to assimilate AOD data at 550 nm. The assimilated AOD observations
335 are including (1) AOD retrievals from AVHRR (1979-2002) over global ocean, (2) AOD retrievals
336 from MODIS on Terra (2000–present) and Aqua (2002–present) over global land and ocean, (3)
337 AOD retrievals from MISR (2000–2014) over bright and desert surfaces, and (4) direct AOD
338 measurements from the ground-based AERONET (1999–2014) (Gelaro et al., 2017). The monthly
339 MERRA-2 AOD is used to evaluate the model’s predictive ability before 2000 and after 2000.

340 **2.7 Decision tree regression**

341 **2.7.1 Feature selection**

342 Although a multidimensional dataset can provide as much potential information as possible for
343 AOD, irrelevant and redundant variables can also introduce significant noise in the model and
344 reduce the model’s accuracy and stability (Kang et al., 2021; Dong et al., 2023). Therefore, the F-
345 test is used to search for the optimal feature subset in the Predictor, aiming to eliminate irrelevant
346 or redundant features and select truly relevant features, which helps to simplify the model’s input
347 and improve the model’s prediction ability (Dhanya et al., 2020). The F-test is a statistical test that
348 gives an f-score ($= -\log(p)$, p represents the degree to which the null hypothesis is not rejected) by
349 calculating the ratio of variances. In this study, we calculate the ratio of variance between the

350 Predictors and Target, and the features are ranked based on the f-score values. A larger value of f-
351 score means that the distances between Predictors and Target are less and the relationship is closer,
352 thus, the feature is more important. We set $p=0.05$. When the score is less than $-\log(0.05)$, the
353 variable in the Predictors is not considered.

354 **2.7.2 Data balance**

355 When the weather is clear, the AOD value is small ($AOD < 0.5$), and the variability of AOD is small, and
356 the data is concentrated near the mean value. When heavy pollution, the AOD value is large ($AOD > 0.5$).
357 Compared to clear sky, the AOD sequence will show "abnormal" large values with low frequency, which
358 is a phenomenon of imbalance AOD data. When dealing with imbalanced datasets, because of the
359 tendency of machine learning algorithms to perform better on the majority class and overlook the
360 minority class, the model may be underfit (Chuang and Huang, 2023). Data augmentation techniques are
361 commonly employed to address the issue in imbalance data, which applies a series of transformations or
362 expansions to generate new training data, thereby increasing the diversity and quantity of the training
363 data of the minority class.

364 The Adaptive Synthetic Sampling (ADASYN) is a data augmentation technique specifically designed to
365 address data imbalance problem (He et al., 2008; Mitra et al., 2023). It is an extension of the Synthetic
366 Minority Over-sampling Technique (SMOTE) algorithm (Fernández et al., 2018). The goal of ADASYN
367 is to generate synthetic sample data for the minority class to increase its representation in the dataset.
368 ADASYN, which adaptively adjusts the generation ratio of synthetic samples based on the density
369 distribution of sample data, improves the dataset balance and enhances the performance of machine
370 learning models in dealing with imbalanced data.

371 The processing of imbalanced data includes (1) AOD sequences are classified into three types based on
372 percentile (0-1%, 2% -98%, 99%), (2) When the mean of the third type of AOD is greater than 5 times
373 the standard bias of the second type, it is considered an imbalanced sequence. These data, with a total
374 amount less than 5% of the sample, are imbalanced data, and (3) Then synthetic samples are generated
375 with a 10% upper limit of the original samples.

376 **2.7.3 Decision tree regression model**

377 The decision tree is a machine learning algorithm based on a tree-like structure used to solve
378 classification and regression problems. We use regression tree algorithm to construct a regression model
379 by analyzing the mapping relationship between object attributes (Predictors) and object values (Target).
380 The internal nodes have binary tree structures with feature values of "yes" and "no". In addition, each
381 leaf node represents a specific output for a feature space. The advantages of the regression tree include
382 the ability to handle continuous features and the ease of understanding the generated tree structure
383 (Teixeira, 2004; Berk, 2008). Before training the tree model, the variables (Input) are normalized to
384 improve model performance, and after prediction, the results are obtained by denormalization. The 10-
385 fold cross-validation method is employed to improve the generalization ability of the model (Browne,
386 2000).

387 The core problems of the regression tree need to be solved are to find the optimal split variable and
388 optimal split point. The optimal split point of Predictors is determined by the minimum MSE, which in
389 turn determines the optimal tree structure. We set $Y = [y_1, y_2, \dots, y_N]$ as the Target. We set $X =$
390 $[x_1, x_2, \dots, x_N]$ as the Predictors, $x_i = (x_i^1, x_i^2, \dots, x_i^n)$, $i = 1, 2, 3, \dots, N$, where n is the feature number, and

391 N is the length of sample. We set a training dataset as $D = [(x_1, y_1), (x_2, y_2), \dots, (x_N, y_N)]$.

392 A regression tree corresponds to a split in the feature space and the output values on the split domains.

393 Assuming that the input space has been divided into M domains $[R_1, R_2, \dots, R_M]$ and there is a fixed

394 output value on each R_M domain, the regression tree model can be represented as follows:

$$395 \quad f(x) = \sum_{m=1}^M c_m I(x \in R_m), \quad m = 1, 2, \dots, M, \quad (4)$$

396 where I is the indicator function, equation (5):

$$397 \quad I = \begin{cases} 1, & x \in R_m \\ 0, & x \notin R_m \end{cases}, \quad (5)$$

398 When the partition of the input space is determined, the square error can be used to represent the

399 prediction error of the regression tree for the training data, and the minimizing square error is used to

400 solve the optimal output value on each domain. The optimal value (\widehat{c}_m) on a domain is the mean of the

401 outputs corresponding to all input, namely:

$$402 \quad \widehat{c}_m = \text{ave}(y_i | x_i \in R_m), \quad (6)$$

403 A heuristic method is used to split the feature space in CART. After each split, all values of all features

404 in the current set are examined individually, and the optimal one is selected as the split point based on

405 the principle of minimum sum of the square errors. The specific step is described as follows: for the

406 training dataset D, we recursively divide each region into two sub domains and calculate the output

407 values of each sub domain; then, construct a binary decision tree. For example, split variable is x^j and

408 split point is s . Then, in the domain $R_1(j, s) = [x | x^j \leq s]$ and domain $R_2(j, s) = [x | x^j > s]$, we can

409 solve the loss function $L(j, s)$ to find the optimal j and s .

$$410 \quad L(j, s) = \sum_{x_i \in R_1(j, s)} (y_i - c_1)^2 + \sum_{x_i \in R_2(j, s)} (y_i - c_2)^2, \quad (7)$$

411 When $L(j, s)$ is the smallest, x^j is the optimal split variable and s is the optimal split point for the

412 x^j .

$$413 \quad \min_{j, s} \left[\min_{c_1} \sum_{x_i \in R_1(j, s)} (y_i - c_1)^2 + \min_{c_2} \sum_{x_i \in R_2(j, s)} (y_i - c_2)^2 \right], \quad (8)$$

414 We use the optimal split variable x^j and the optimal split point s to split the feature space and calculate

415 the corresponding output value.

$$416 \quad \widehat{c}_1 = \text{ave}(y_i | x_i \in R_1(j, s)), \quad \widehat{c}_2 = \text{ave}(y_i | x_i \in R_2(j, s)), \quad (9)$$

417 We traverse all input variables to find the optimal split variable x^j , forming a pair (j, s) . Divide the

418 input space into two regions accordingly. Next, repeat the above process for each region until the stop

419 condition is met. The regression tree is generated.

420 Therefore, the regression tree model $f(x)$ can be represented as follows:

$$421 \quad f(x) = \sum_{m=1}^M \widehat{c}_m I(x \in R_m), \quad m = 1, 2, \dots, M, \quad (10)$$

422 2.8 Evaluation metrics

423 Evaluation metrics, including Root Mean Squared Error (RMSE), Mean Absolute Error (MAE) and

424 Pearson Correlation Coefficient (R), are used to measure the performance and accuracy of the model
 425 results.

$$426 \quad RMSE = \sqrt{\frac{1}{n} \sum_{i=1}^n (y_i - \hat{y}_i)^2}, \quad (11)$$

$$427 \quad MAE = \frac{1}{n} \sum_{i=1}^n |y_i - \hat{y}_i|, \quad (12)$$

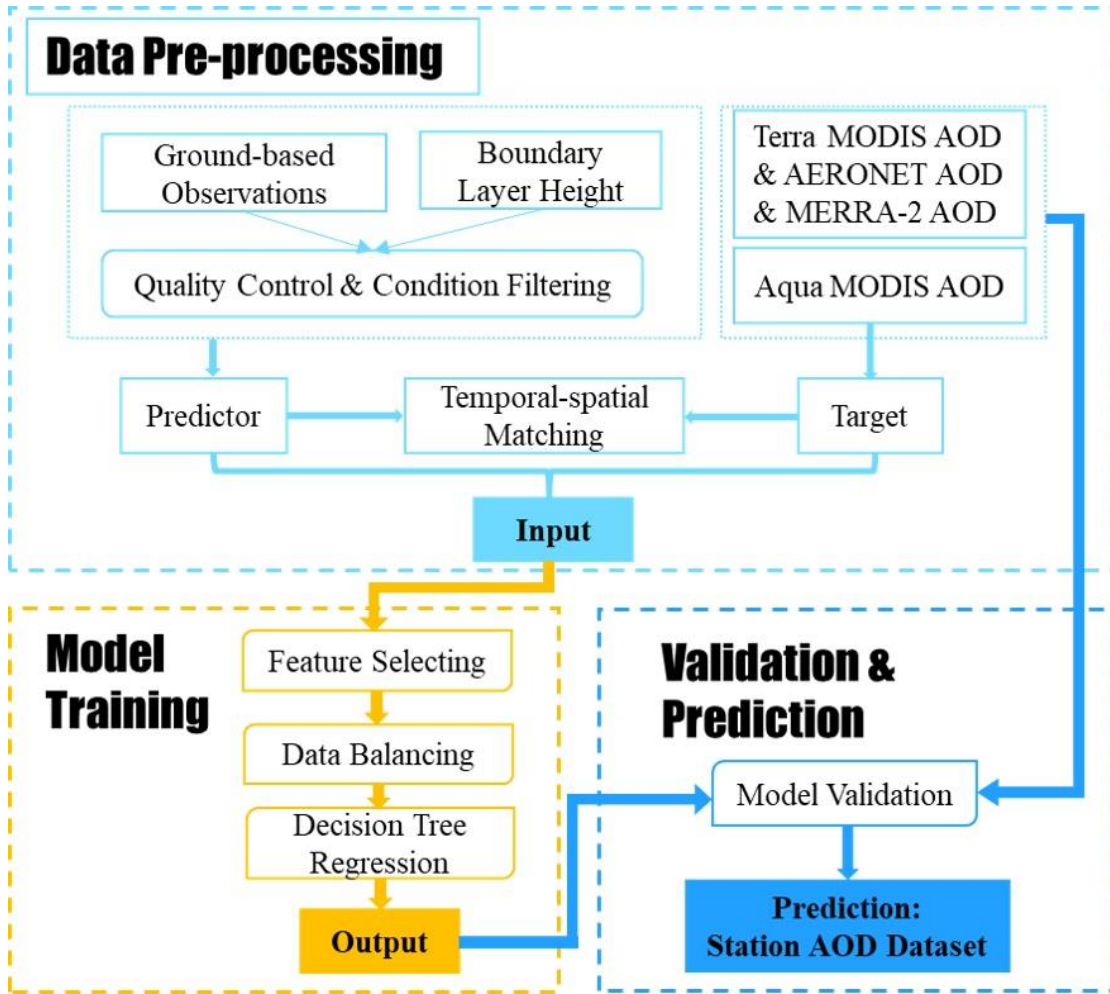
$$428 \quad R = \frac{\sum_{i=1}^n (y_i - \bar{y})(\hat{y}_i - \bar{\hat{y}})}{\sqrt{(\sum_{i=1}^n (y_i - \bar{y})^2 \sum_{i=1}^n (\hat{y}_i - \bar{\hat{y}})^2)}}, \quad (13)$$

429 where y_i and \bar{y} are the predicted value and the average of the predicted values. \hat{y}_i and $\bar{\hat{y}}$ are
 430 the target and the average of the target. $i = 1, 2, \dots, n$. n is the length of sample.

431 The expected error (EE) is used to evaluate the AOD derived from visibility.

$$432 \quad EE = \pm(0.05 + 0.15 * \tau_{true}), \quad (14)$$

433 where τ_{true} is the AOD at 550 nm from AERONET, satellite and reanalysis datasets.



434
 435 **Figure 2:** Flowchart for deriving aerosol optical depth (AOD).

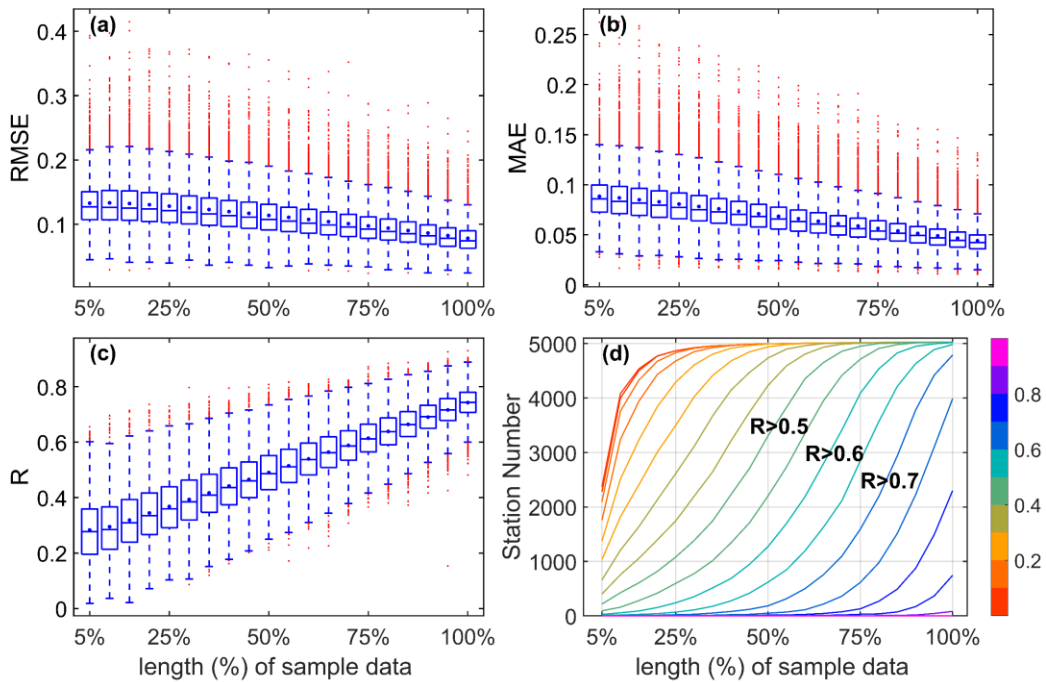
436 **2.9 Workflow**

437 Figure 2 summarizes the flowchart and provides an overview of the structure of this study, which
 438 involves four main parts: (1) data preprocessing, (2) model training, and (3) validation and
 439 prediction.

440 3 Results and discussion

441 3.1 Dependence of model performance on training data length

442



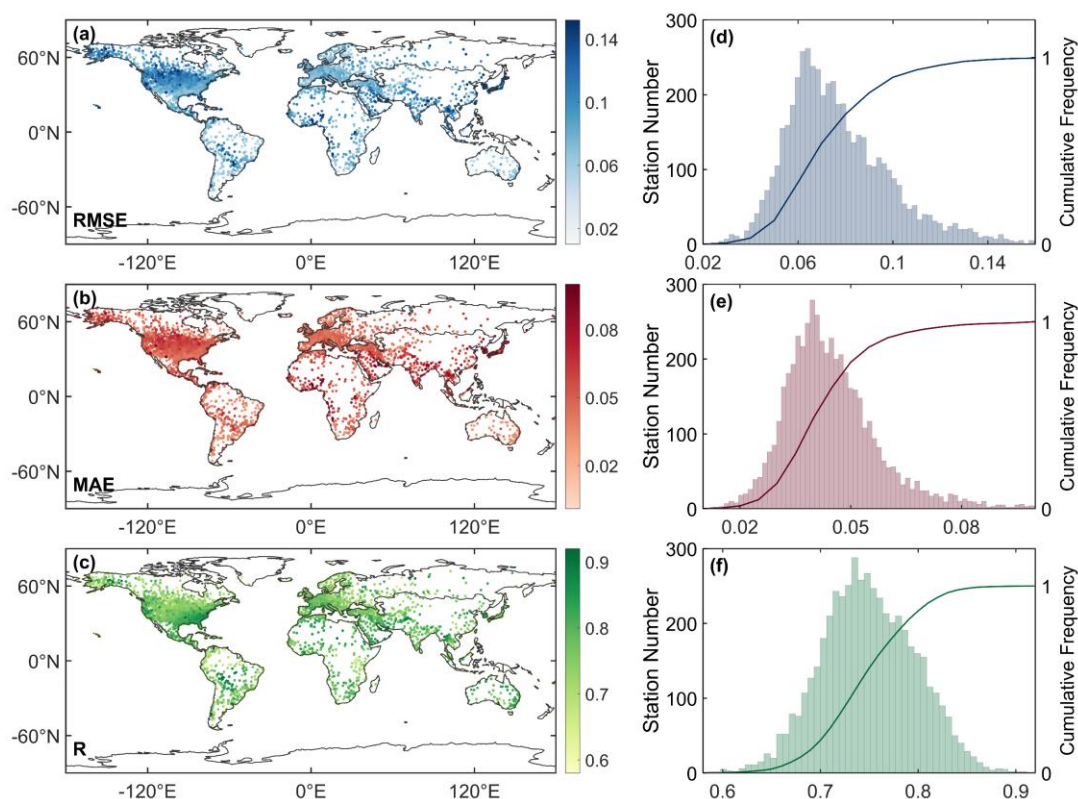
443

444 **Figure 3:** Boxplots of root mean squared error (RMSE) (a), mean absolute error (MAE) (b), and
 445 correlation coefficient (R) (c) between predicted values and target using different lengths of sample
 446 data (5% interval) as the training dataset, and the correlation coefficient curve (d) of the station
 447 number and lengths of sample data.

448 We build the models using different lengths of sample data (5% to 100%, with a 5% interval) by random
 449 allocation without overlap and evaluate the predictive performance of each model. Figure 3 (a-c) depicts
 450 RMSE, MAE, and R between the predicted values and target based on the training data of 5% to 100%
 451 sample data at a station. As the volume of the training data increases, the RMSE and MAE values
 452 decrease, and the R values increase. Compared to 5% of the sample data, the result of 100% sample data
 453 shows a decrease in RMSE by 41.1%, a decrease in MAE by 50.1%, and an increase in R by 162.3%.
 454 The relationship between the length of sample data and the model's performance is positive for each
 455 station. Figure 3 (d) shows that R of approximately 70% stations is greater than 0.5 at 50% of the sample
 456 data, while at 75%, the R of approximately 80% of stations is greater than 0.6. When 100% of the sample
 457 data is used as sample data, the R of approximately 80% of stations is greater than 0.75, and the R of
 458 about 97% is greater than 0.7. This finding indicates that the predictive capability and robustness of the
 459 model increase as the amount of training data increases. It may be attributed to the model's ability to
 460 capture more complex patterns and relationships among the input by multi-year data.

461 3.2 Evaluation of model training performance

462 Figure 4 shows the spatial distribution (a-c) and frequency and cumulative frequency (d-e) of RMSE,
463 MAE, and R of all stations. The mean values of RMSE, MAE and R are 0.078, 0.044, and 0.750,
464 respectively. The RMSE of 93% stations is less than 0.11, the MAE of 91% is less than 0.06, and the R
465 of 88% is greater than 0.7. The R values in Africa, Asia, Europe, North America, Oceania, and South
466 America are 0.763, 0.758, 0.736, 0.750, 0.759, and 0.738, respectively. Although the RMSE and MAE
467 of a few stations are high in America and Asia, the R is still high (>0.6). Therefore, the results of the
468 model's errors demonstrate that the model performs well on almost all stations.



469

470 **Figure 4:** Spatial distribution (a-c) of root mean squared error (RMSE), mean absolute error (MAE),
471 and correlation coefficient(R) between the model's result and target with 100% sample data. Station
472 number (bar) and cumulative frequency (curve) (d-e) of RMSE, MAE, and R.

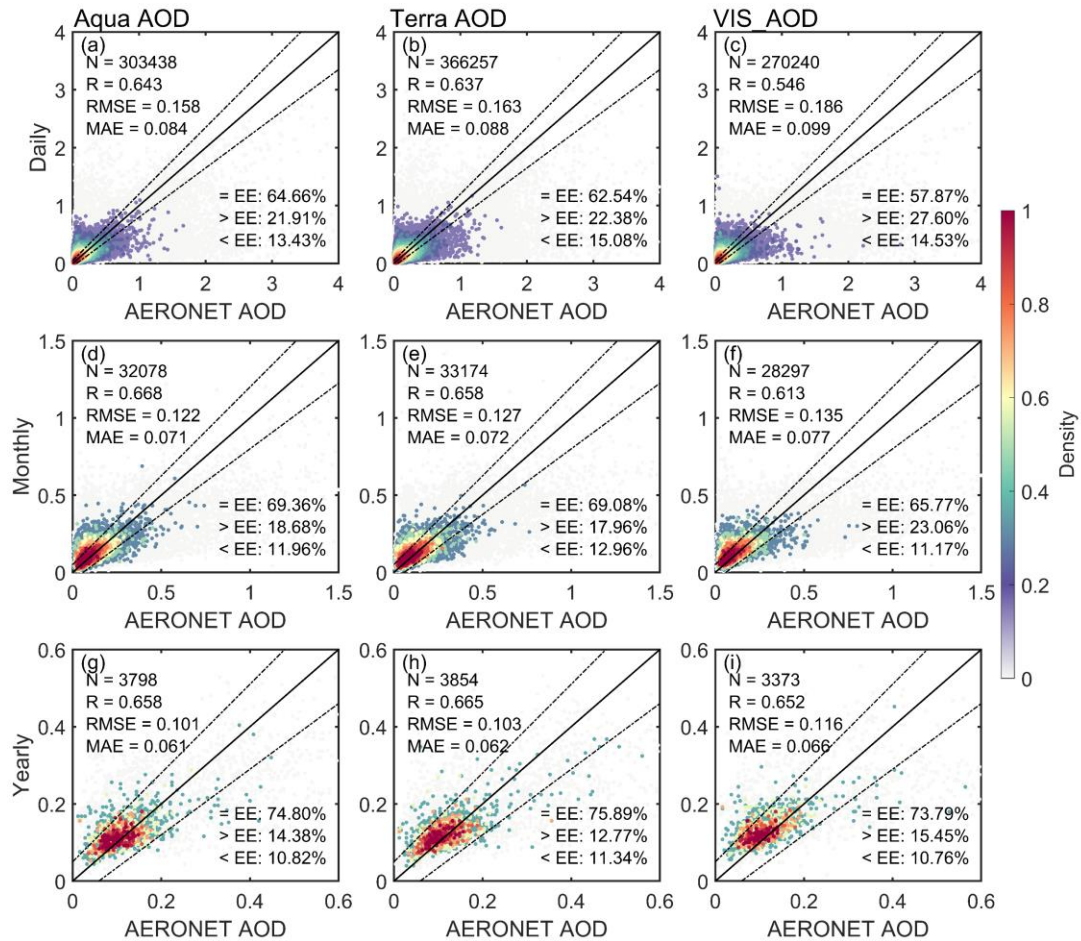
473 3.3 Validation and comparison with MODIS and AERONET AOD

474 3.3.1 Validation over global land

475 To validate the model's predictive ability, the visibility-derived AOD (for short, VIS_AOD) is compared
476 with Aqua, Terra, MERRA-2 and AERONET AOD at 550nm for the global scale. Among them, Aqua
477 AOD has been used as training data, which is not independent. Terra AOD and AERONET AOD have
478 not been used as training data and can be regarded as independent data.

479 First, the relationship among daily MODIS and AERONET AOD is evaluated, as shown in Figure 5 (a-
480 b, d-e, g-h). The R values with Aqua AOD and Terra AOD are 0.643 and 0.637 on the daily scale, and
481 0.668 and 0.658 on the monthly scale, 0.658 and 0.665 on the yearly scale. The RMSE with Aqua AOD
482 and Terra AOD are 0.158 and 0.163 on the daily scale, and 0.122 and 0.127 on the monthly scale, 0.101

483 and 0.103 on the yearly scale. The MAE values with Aqua AOD and Terra AOD are 0.084 and 0.088 on
 484 the daily scale, and 0.071 and 0.072 on the monthly scale, 0.061 and 0.062 on the yearly scale. The
 485 percentages of sample point falling within the EE envelopes are 64.66% and 62.54% on the daily scale,
 486 and 69.36% and 69.08% on the monthly scale, 74.80% and 75.89% on the yearly scale.



487

488 **Figure 5:** Scatter density plots between AERONET AOD (550nm) and Aqua MODIS AOD, Terra
 489 MODIS AOD and VIS_AOD on the daily (a-c), monthly (d-f) and yearly (g-i) scale. The solid black line
 490 represents the 1:1 line and the dashed lines represents expected error (EE) envelopes. The sample size
 491 (N), correlation coefficient (R), mean absolute error (MAE), and root mean square error (RMSE) are
 492 given. ‘= EE’, ‘> EE’, and ‘< EE’ represent the percentages (%) of retrievals falling within, above, and
 493 below the EE, respectively. The matching time for Aqua AOD and VIS_AOD with AERONET AOD is
 494 13.30 (\pm 30 minutes) at local time, and the matching time between Terra AOD and AERONET AOD is
 495 10.30 (\pm 30 minutes) at local time.

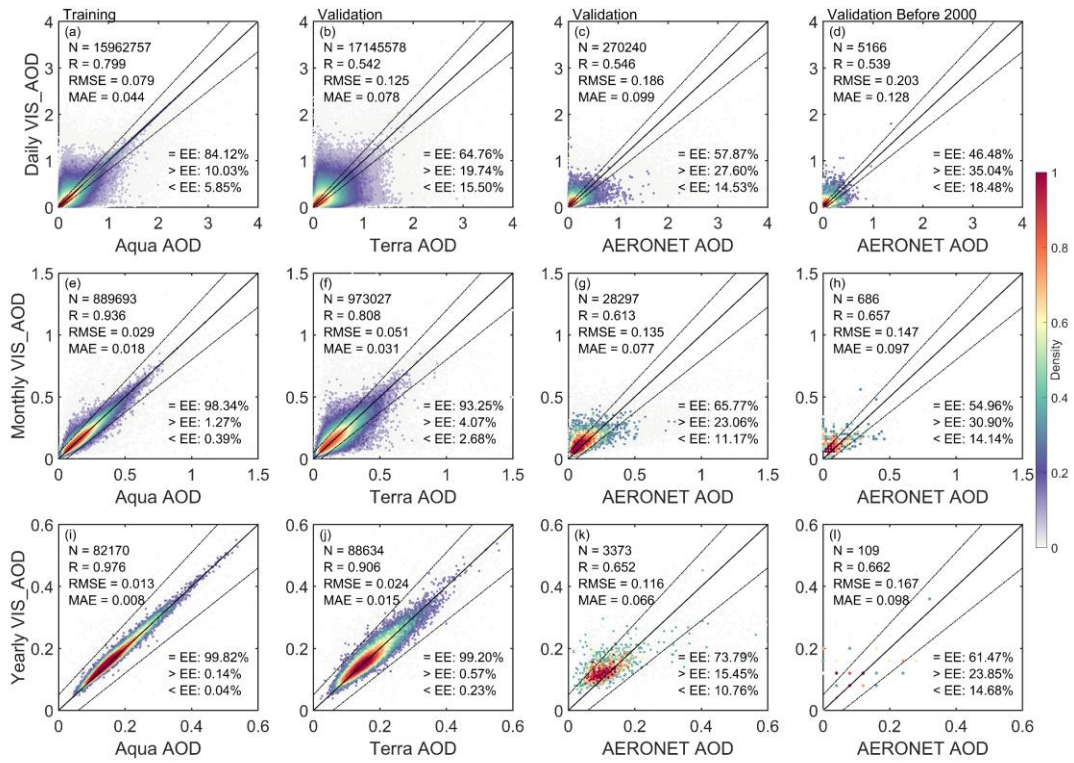
496 Figure 6 shows the scatter density plots and the EEs between VIS_AOD and Aqua AOD, Terra AOD,
 497 and AERONET AOD. Aqua AOD is not an independent validation, and Terra and AERONET AOD are
 498 independent validation. For the daily scale, the R, RMSE and MAE of between VIS_AOD and Aqua
 499 AOD (15,962,757 pairs data) is 0.799, 0.079 and 0.044, respectively. The percentage of sample point
 500 falling within the EE envelopes is 84.12% on the global scale (Figure 6 a). The R between VIS_AOD
 501 and Terra AOD (17,145,578 pairs data) is 0.542, with a RMSE of 0.125 and MAE of 0.078. The
 502 percentage falling within the EE envelopes is 64.76% (Figure 6 b). The R between VIS_AOD and

503 AERONET AOD (270,240 pairs data) at 395 sites is 0.546, with a RMSE of 0.186 and MAE of 0.099.
504 The percentage falling within the EE envelopes is 57.87% (Figure 6 c).

505 For the monthly and annual scales, RMSE and MAE show a significant decrease between VIS_AOD and
506 Aqua, Terra, and AERONET AOD, and R and percentages falling within EE show a significant increase
507 in Figure 6 (e-g, i-k). The monthly RMSEs are 0.029, 0.051, and 0.135, the monthly MAEs are 0.018,
508 0.031, and 0.077, and the monthly R values are 0.936, 0.808, and 0.613, respectively. The percentages
509 falling within the EE envelopes are 98.34%, 93.25%, and 65.77%. The RMSEs on the yearly scale are
510 0.013, 0.024, and 0.116, the MAEs are 0.008, 0.015, and 0.066, and the R values are 0.976, 0.906, and
511 0.652, respectively. The percentages falling within the EE envelopes are 99.82%, 99.20%, and 73.79%.
512 The percentage falling within the EE envelopes against AERONET is smaller than that against Terra,
513 which may be related to the elevation of AERONET sites, the distance between AERONET and
514 meteorological stations, and observed time. The results highlighted above demonstrate a clear
515 improvement in performance on the monthly and yearly scales compared to the daily scale.

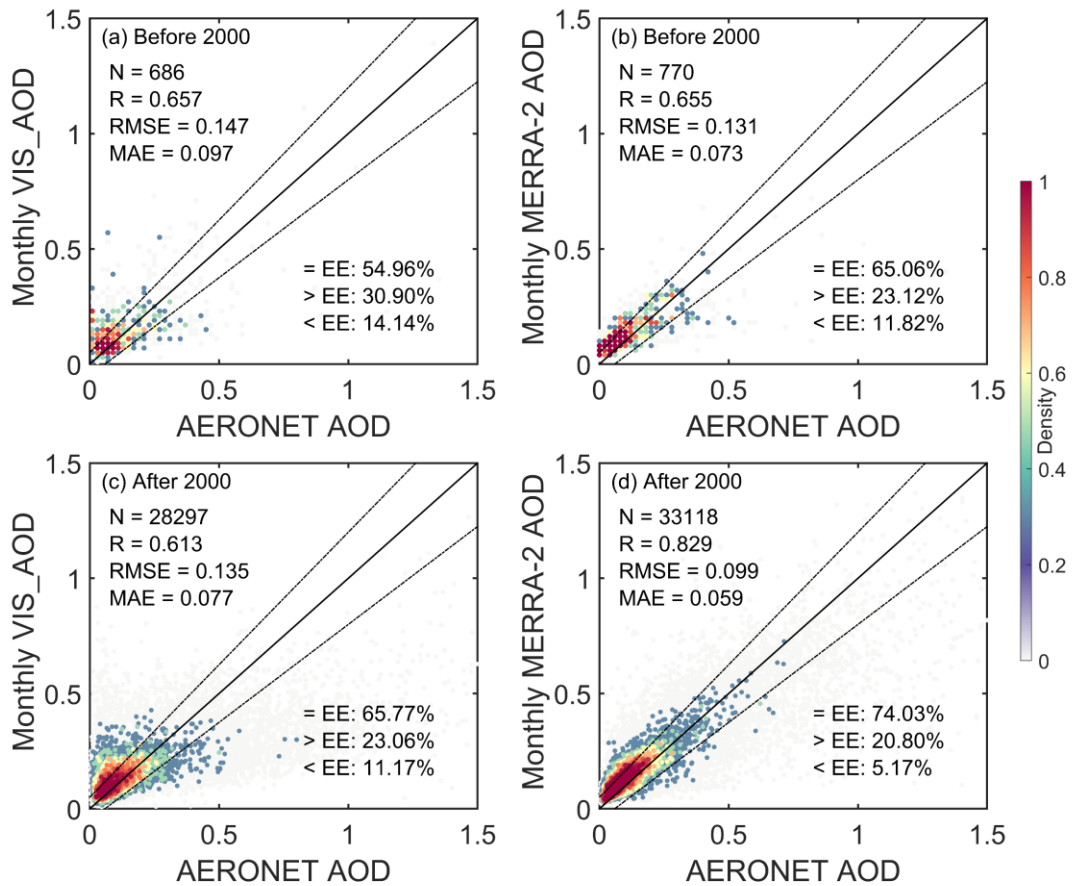
516 To further examine the predictive capability of historical data, we compare the VIS_AOD with
517 AERONET AOD before 2000, as shown in Figure 6 (d, h, l). We match 43 AERONET sites, with a total
518 of 5166 daily records. The result indicates that the daily-scale R is close to that after 2000 (Figure 6 c),
519 with the percentages approaching 50% falling within the EE envelopes. The monthly and annual
520 correlation coefficients are even higher, with a percentage of 55% falling within the EE envelopes.
521 Although the sample size is small, it still demonstrates the excellent predictive ability of the model.
522 Compared with AERONET (an independent validation dataset), the performance of VIS_AOD is almost
523 unchanged before and after 2000.

524 We also compare the VIS_AOD with the MERRA-2 reanalysis AOD on the monthly scale, as shown in
525 Figure 7. The correlation coefficient between MERRA-2 and AERONET is 0.655 before 2000, slightly
526 lower than the correlation coefficient (0.657) between VIS_AOD and AERONET. The correlation
527 coefficient between MERRA-2 and AERONET is 0.829 after 2000, significantly higher than that before
528 2000, while the correlation coefficient between VIS_AOD and AERONET is 0.613. It suggests that
529 VIS_AOD and MERRA-2 AOD have similar accuracy before 2000. The correlation of MERRA-2 after
530 2000 is higher and even performs better than MODIS retrievals (as shown in Figure 5) when evaluated
531 at AERONET sites. However, before 2000, the correlation coefficient of MERRA-2 and AERONET,
532 RMSE, and MAE all show significant changes and differences in consistency. The higher correlation
533 between MERRA-2 and AERONET AOD is partly because MERRA-2 has assimilated AERONET AOD
534 observations (Gelaro et al., 2017). Compared to AERONET, VIS_AOD and Aqua/Terra MODIS have a
535 similar correlation coefficient. The correlation coefficient of VIS_AOD before 2000 is even higher than
536 after 2000, and the changes in RMSE and MAE are not significant. It indicates good consistency of
537 VIS_AOD. In conclusion, the predicted results have good consistency with AERONET AOD and Terra
538 AOD on the daily scale. The monthly and annual results have a significant improvement. The model
539 shows good predictive capabilities before/after 2000, highlighting the stable accuracy of VIS_AOD.



540

541 **Figure 6:** Scatter density plots between predicted AOD (VIS_AOD) and Aqua MODIS AOD, Terra
 542 MODIS AOD, AERONET AOD and AERONET AOD before 2000 on the daily (a-d), monthly (e-h) and
 543 yearly (g-i) scale. The solid black line represents the 1:1 line and the dashed lines represents expected
 544 error (EE) envelopes. The sample size (N), correlation coefficient (R), mean absolute error (MAE), and
 545 root mean square error (RMSE) are given. ‘= EE’, ‘> EE’, and ‘< EE’ represent the percentages (%) of
 546 retrievals falling within, above, and below the EE, respectively. Note Aqua AOD is not an independent
 547 validation dataset for predicted results, while Terra and AERONET AOD are independent validation
 548 datasets.



549

550 **Figure 7:** Scatter density plots between AERONET AOD and the predicted AOD (VIS_AOD) and
 551 MERRA-2 AOD before/after 2000 on the monthly scale. The solid black line represents the 1:1 line and
 552 the dashed lines represents expected error (EE) envelopes. The sample size (N), correlation coefficient
 553 (R), mean absolute error (MAE), and root mean square error (RMSE) are given. ‘= EE’, ‘> EE’, and ‘<
 554 EE’ represent the percentages (%) of retrievals falling within, above, and below the EE, respectively.

555 3.3.2 Validation over regions

556 Aerosol loading exhibits spatial variability. Evaluation metrics for the relationships between
 557 visibility-derived AOD and AERONET AOD and Terra AOD for each region are listed in Table 1.
 558 In Europe and North America, the results are similar to those of Terra and AERONET, with a large
 559 number of data pairs, greater than 10^5 (AERONET) and greater than 10^7 except for Eastern Europe
 560 (Terra) on the daily scale. Approximately 63% -70% data pairs fall within the EE envelopes. The
 561 RMSE is approximately 0.11, except for western North America (~ 0.15), and the MAE is
 562 approximately 0.07, and the correlation coefficient is between 0.44 and 0.54.

563 In Central South America, South Africa, and Australia, data pairs are about 10^{3-4} (AERONET) and
 564 10^6 (Terra) on the daily scale. 52-60% fall within the EE envelopes compared to AERONET, and
 565 58-67% compared to Terra. The RMSE is 0.03-0.05 compared to Terra, and 0.11-0.17 compared to
 566 AERONET. The correlation coefficient ranges from 0.40 to 0.74, with the highest correlation
 567 coefficient in South America at 0.74.

568 In Asia, India, and West Africa, the data pairs are only approximately 10^4 (AERONET). 32% to 50%

569 fall within the EE envelopes compared to AERONET, the RMSE value ranges from 0.20 to 0.50,
570 and the MAE ranges from 0.11 to 0.36. Compared to Terra AOD, 51 to 58% of data pairs fall within
571 the EE envelopes, the RMSE is around 0.16, and the MAE is around 0.11. Compared to AERONET,
572 in these high aerosol loading regions, RMSE and MAE increase, and the percentages falling within
573 the EE envelopes decrease, but the correlation coefficients do not significantly decrease.
574 Compared to Terra AOD, 55% -67% of data falls within the EE envelopes on the daily scale, 87% -
575 96% on the monthly scale, and over 97% on the yearly scale. Compared to AERONET AOD, 32-
576 68% of data falls within the EE envelopes, 24% -84% on the monthly scale, and 15% -97% on the
577 yearly scale. On both monthly and yearly scales, all metrics have shown a significant increase in
578 performance when compared to Terra. However, compared to AERONET, not all metrics increase
579 in some regions due to limited data pairs, such as West Africa, Northeast Asia, and India, which may
580 be due to the spatial differences between AERONET sites and meteorological stations.

581 **3.3.3 Validation at a site scale**

582 Sites, especially AERONET, are not completely uniform across the world or in any region, and
583 different stations have different sample sizes, which may lead to a certain uncertainty. Therefore,
584 further analysis is conducted on the spatial distribution of different evaluation metrics. Figure 8
585 shows the validation and comparison of daily VIS_AOD against Terra and AERONET AOD at a
586 site scale.

587 Compared to Terra daily AOD, the R of 67% stations is greater than 0.40, the mean bias of 83% is

Table 1: Evaluation metrics for the relationships between visibility-derived AOD and AERONET AOD and Terra AOD for each region.

Region		N			R			RMSE			MAE			Within EE (%)		
		daily	monthly	yearly	daily	monthly	yearly	daily	monthly	yearly	daily	monthly	yearly	daily	monthly	yearly
Eastern Europe	AERONET	21724	2317	271	0.463	0.493	0.653	0.1069	0.0647	0.0326	0.0714	0.0442	0.0263	65.69	83.77	97.42
	TERRA	661630	36435	3278	0.464	0.665	0.790	0.1095	0.0471	0.0214	0.0726	0.0286	0.0122	66.07	94.71	99.18
Western Europe	AERONET	53043	6033	697	0.445	0.487	0.344	0.1089	0.0716	0.0513	0.0711	0.0474	0.0347	64.40	79.21	89.10
	TERRA	1778013	104620	9166	0.467	0.763	0.811	0.1096	0.0391	0.0210	0.0712	0.0268	0.0124	66.99	95.42	99.40
Western North America	AERONET	33859	2948	334	0.503	0.484	0.509	0.1465	0.0949	0.0566	0.0747	0.0597	0.0419	63.58	67.37	81.14
	TERRA	1725226	82734	7201	0.542	0.765	0.906	0.1144	0.0465	0.0180	0.0671	0.0267	0.0125	69.48	94.42	99.61
Eastern North America	AERONET	47407	5359	608	0.527	0.526	0.559	0.1135	0.0824	0.0436	0.0657	0.0472	0.0331	67.52	77.78	87.50
	TERRA	6280277	359520	31343	0.515	0.799	0.847	0.1159	0.0435	0.0165	0.0726	0.0275	0.0111	66.70	94.94	99.80
Central South America	AERONET	10911	1176	149	0.740	0.811	0.866	0.1735	0.1272	0.1060	0.1021	0.0904	0.0688	52.40	47.96	67.79
	TERRA	444780	26362	2410	0.545	0.820	0.776	0.1447	0.0591	0.0369	0.0909	0.0396	0.0219	58.48	89.29	97.39
Southern Africa	AERONET	4255	309	38	0.423	0.480	0.630	0.1553	0.1128	0.0705	0.1033	0.0805	0.0525	52.08	59.55	78.95
	TERRA	216239	11304	1118	0.518	0.821	0.870	0.1258	0.0511	0.0296	0.0836	0.0340	0.0191	60.64	91.70	98.21
Australia	AERONET	6426	516	63	0.488	0.654	0.363	0.1094	0.0827	0.0725	0.0711	0.0620	0.0563	59.96	59.88	71.43
	TERRA	284693	14588	1286	0.398	0.784	0.831	0.1091	0.0363	0.0188	0.0666	0.0261	0.0143	67.01	94.65	99.38
Western Africa	AERONET	2205	205	34	0.553	0.594	0.762	0.3180	0.2873	0.3357	0.2082	0.2029	0.2587	37.96	40.00	23.53
	TERRA	156392	10468	1028	0.501	0.769	0.849	0.1769	0.0706	0.0412	0.1198	0.0482	0.0242	51.83	88.01	97.57
Southeast Asia	AERONET	4134	504	74	0.405	0.542	0.488	0.2037	0.1447	0.1198	0.1274	0.0988	0.0821	50.17	56.15	60.81
	TERRA	402465	27058	2500	0.470	0.753	0.872	0.1730	0.0729	0.0342	0.109	0.0455	0.0198	57.25	87.01	97.96
Eastern China	AERONET	7396	927	118	0.513	0.551	0.356	0.3571	0.2355	0.1933	0.2038	0.1392	0.1382	40.10	49.84	50.00
	TERRA	241185	17324	1518	0.523	0.811	0.895	0.1646	0.0638	0.0302	0.1073	0.0435	0.0225	55.77	88.07	98.88
Northeast Asia	AERONET	9979	1178	142	0.569	0.593	0.367	0.4941	0.3249	0.2604	0.2924	0.2425	0.2202	35.17	29.54	21.13
	TERRA	78823	5485	467	0.553	0.872	0.965	0.1973	0.0636	0.0263	0.1201	0.0440	0.0198	56.48	87.77	98.29

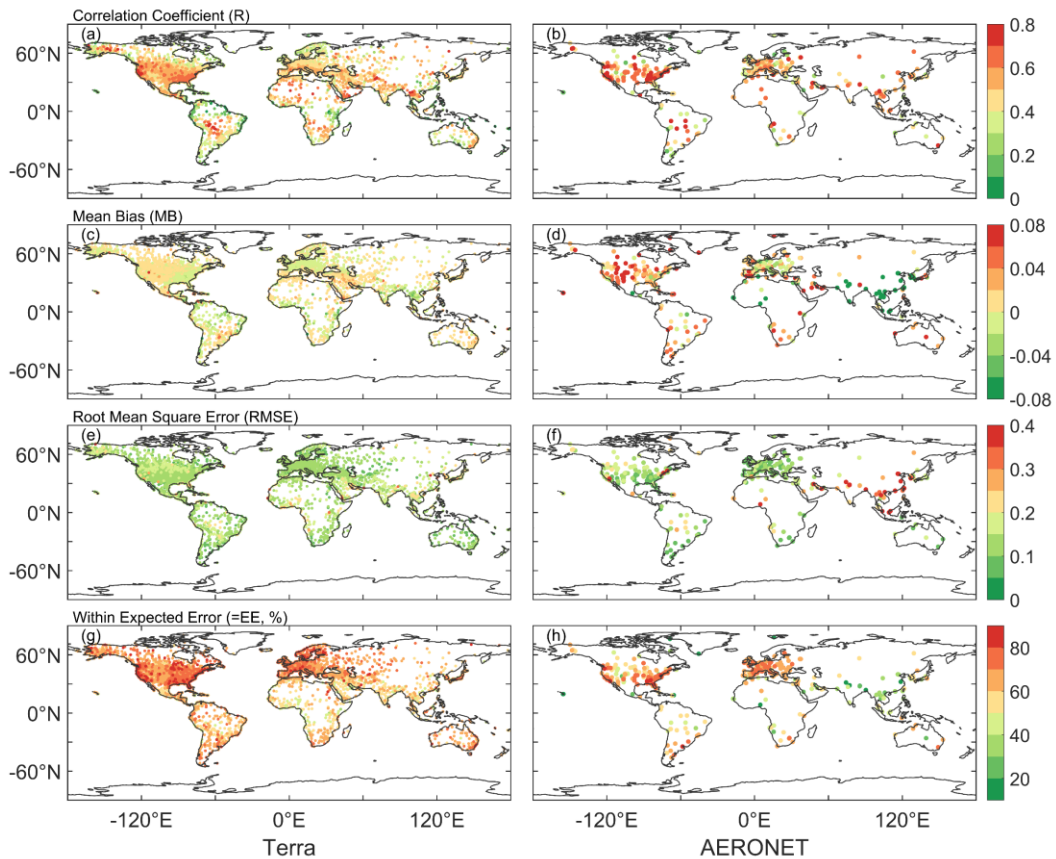
<i>India</i>	<i>AERONET</i>	2208	203	32	0.521	0.462	0.534	0.2957	0.3015	0.3588	0.2049	0.2283	0.2862	32.11	24.63	15.63
	<i>TERRA</i>	179928	9564	862	0.526	0.815	0.915	0.1564	0.0599	0.0352	0.1089	0.042	0.0238	55.16	90.43	98.14

589

590 less than 0.01, the RMSE of 85% is less than 0.15, and the percentage falling within the EE of 67%
591 is greater than 60%. More than 85% of stations fall within the EE is greater than 60% in Europe,
592 North America, and Oceania, while 40-60% in South America, Africa, and Asia. The percentage of
593 expected error is low in South and East Asia, and Central Africa, with some underestimation. Above
594 60% in Africa, Asia, North America, and Europe have a correlation coefficient greater than 0.40.
595 The regions with lower correlation are the coastal regions of South America, eastern Africa, western
596 Australia, northeastern North America, and northern Europe. Above 90% of the RMSE in Europe,
597 North America, and Oceania have a correlation coefficient smaller than 0.15. High RMSE regions
598 are in western North America, Asia, central South America, and central Africa.

599 Compared to AERONET daily AOD, the R of 74% stations is greater than 0.40, and the spatial
600 distribution is similar to Terra's. The mean bias of 44% is less than 0.01, the RMSE of 68% is less
601 than 0.15, and the percentage falling within the EE of 53% is greater than 60%. More than 70% of
602 sites have a correlation coefficient greater than 0.40 in Africa, Asia, Europe, and North America.
603 More than 57% of sites have an expected error percentage of over 60% in Europe, North America,
604 and Oceania, except for Asia. Over 72% of sites have a RMSE less than 0.15. Except for Oceania
605 and South America, over 71% of sites in other regions have MAE less than 0.01. Almost all sites in
606 Asia show a negative bias, significantly underestimating. However, there is a significant
607 overestimation in western North America and western Australia. Most sites in Asia falling within
608 the expected error are less than 50%. High RMSE are in high emission and dust areas, such as Asia,
609 India, and Africa.

610 The validation and comparison on the site scale show a limitation similar to the MODIS DT
611 algorithm. In areas with high vegetation coverage, the AOD from visibility are better than those in
612 bright areas. Although the correlation coefficients are high in high aerosol loading areas (Central
613 South America, West Africa, India, Eastern China, Northeast Asia), there are significant differences
614 in these areas with high RMSE values. As shown in Figure 6, some stations located in dusty and
615 urban areas are overestimated or underestimated. Studies have shown that there is a significant
616 uncertainty in the MODIS retrievals in these regions, and the challenges of inversion algorithms are
617 significant in bright surfaces (desert and snow covered areas) and urban surface of densely
618 populated complex structures (Chu et al., 2002; Remer et al., 2005; Levy et al., 2010; Wei et al.,
619 2019; Wei et al., 2020). In India, the elevation difference between AERONET site and
620 meteorological station reached 0.7km may be a factor affecting the validation effect, as aerosol
621 varies greatly with altitude. In eastern China, the complex urban surface, emission sources, and
622 observations in different locations (AERONET site and meteorological station) may be the reasons
623 for underestimation. At the same time, visibility stations in desert areas are sparse, and the spatial
624 variability of dust aerosols is large, which also increases the difficulty to estimate VIS_AOD.



625
 626 **Figure 8:** Validation of VIS_AOD against Terra and AERONET AODs at each site: (a–b)
 627 correlation (R), (c–d) mean bias (MB), (e–f) root mean square error (RMSE), (g–h) percentage (%)
 628 of VIS_AOD within the expected error envelopes.

629 3.3.4 Discussion and uncertainty analysis

630 The atmospheric visibility is a horizontal physical quantity, while AOD is a column-integrated
 631 physical quantity. We have linked the two variables together using machine a learning method,
 632 which partially compensates for the scarcity of AOD data. However, we have to face some
 633 limitations. Although the boundary layer height is considered, it is not sufficient. Pollutants such as
 634 smoke from biomass burning, dust, volcanic ash, and gas-aerosol conversion of sulfur dioxide to
 635 sulfate aerosols in the upper and lower troposphere can undergo long-range aerosol transport under
 636 the influence of circulation. The pollution transport and aerosol conversion processes above the
 637 boundary layer are still significant and cannot be ignored (Eck et al., 2023). Compared to surface
 638 visibility, bias occurs when the aerosol layer rises and affects AERONET measurements and
 639 MODIS retrievals. Therefore, it should be considered when using this data. If there were sufficient
 640 historical vertical aerosol measurements with high temporal and spatial resolution, the results of this
 641 data would be greatly improved. Although some studies use aerosol profiles from pollution transport
 642 models or assumed profiles as substitutes for observed profiles (Li et al., 2020; Zhang et al., 2020),
 643 the biases introduced by these non-observed profiles are still significant.

644 In machine learning, we use MODIS Aqua AOD as the target value for the model because the
 645 validation results for MODIS C6.1 product have a correlation coefficient of 0.9 or higher with
 646 AERONET AOD on the daily scale (Wei et al., 2019; Wei et al., 2020). Compared to AERONET,
 647 MODIS AOD provides more sample data with a high global coverage. However, apart from

648 modeling errors, the systematic biases and uncertainties of MODIS Aqua AOD cannot be ignored
649 (Levy et al., 2013; Levy et al., 2018; Wei et al., 2019). Averaging over time scale can reduce
650 representation errors effectively, and emission sources and orography can increase representation
651 errors (Schutgens et al., 2017). Therefore, the strong correlation at monthly and annual scales
652 indicates a substantial reduction in errors. This is also one of the reasons why this dataset shows
653 stronger correlation with Terra AOD and weaker correlation with AERONET in validation.

654 The spatial matching between meteorological stations and AERONET sites may cause some biases.
655 AERONET sites are usually not co-located with meteorological stations in terms of elevation and
656 horizontal distance, this is another reason for the weak correlation between VIS_AOD and
657 AERONET AOD. The meteorological stations are located at the airport. Different horizontal
658 distances may result in meteorological stations and AERONET sites being located on different
659 surfaces (such as urban, forest, mountainous). Differences in site elevation significantly impact the
660 relationship between AOD and measured visibility. When the AERONET site is at a higher elevation
661 than the meteorological station, there may be fewer measurements of aerosols over the sea at the
662 AERONET site.

663 Different pollution levels and station elevation affect the AOD derived from visibility. The elevation
664 difference and distance between meteorological stations and AERONET sites also have an impact
665 on the validation results. Therefore, the error and performance of different AERONET AOD values,
666 station elevation, and distance are analyzed.

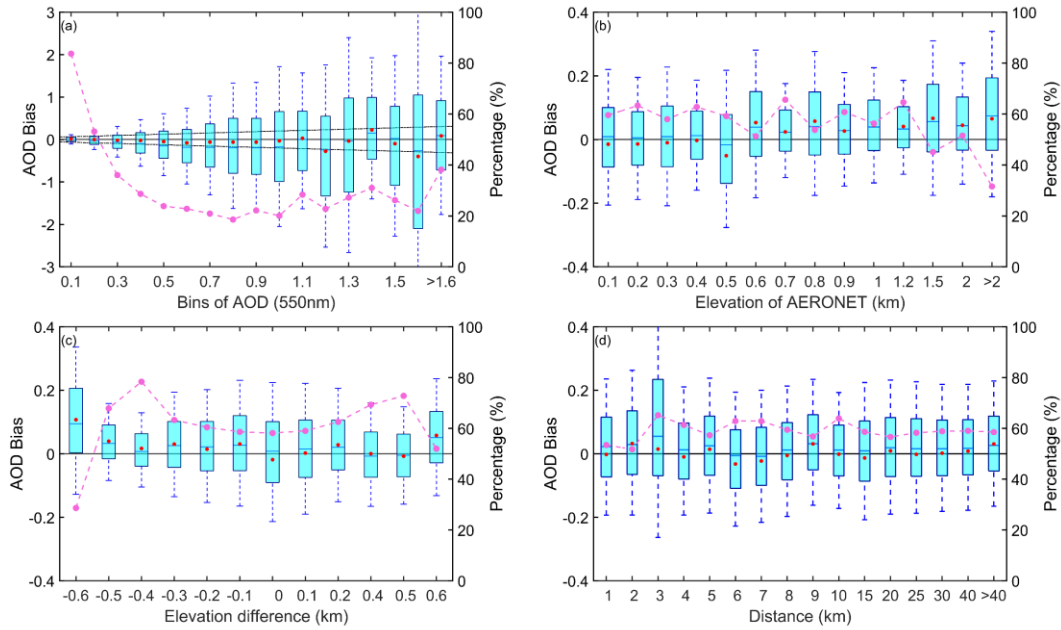
667 As the AOD increases, the variability of bias also increases in Figure 9 (a). Almost all mean bias
668 values are within the envelope of EE, except for 1.1-1.2 and 1.5-1.6. The average bias is 0.015
669 (AOD < 0.1), with 83% of data within the EE envelopes. The mean bias is -0.0011 (AOD, 0.1-0.2),
670 with 54% within the EE envelopes. The mean bias is negative (AOD, 0.3-1.0), with 20%-40%
671 falling within the EE envelopes. There is a positive bias (AOD, 1.1, 1.4 and >1.6), and there is a
672 negative bias at 1.2-1.3 and 1.5-1.6. The results indicate that as pollution level increases, the
673 negative mean bias becomes significant and the underestimation increases.

674 The contribution of particulate matter near the ground to the column aerosol loading is significant.
675 The elevation of the site affects the measurement of column aerosol loading in Figure 9 (b). There
676 is a negative bias in the low elevation (≤ 0.5 km) with a percentage of 60%-64% falling within the
677 EE envelopes and a positive bias in high elevation (0.5-1.2km) with a percentage of 50%-65%
678 falling within the EE envelopes. The percentage significantly decreases (> 1.2 km), and the average
679 bias increases. Therefore, the elevation of AERONET's site will cause bias in validation, and the
680 uncertainty greatly increases in high elevation.

681 Due to the elevation difference between the meteorological station and AERONET site in the
682 vertical direction, the uncertainty caused by elevation differences of site was analyzed in Figure 9
683 (c). When the elevation difference is negative (the elevation of the meteorological station is lower
684 than that of the AERONET station), there is a significant positive bias. When the difference is
685 positive, the mean bias approaches 0 or is positive. The percentage is greater than 60% (-0.5 km-
686 0.5km). The positive mean bias is greater than the negative mean bias, and the uncertainty greatly
687 increases when the elevation of meteorological stations is lower than that of AERONET sites. It
688 indicates that the contribution of the near surface aerosol to the column aerosol loading is significant
689 and cannot be ignored.

690 The spatial variability of aerosols is significant. Meteorological stations and AERONET sites are
691 not collocated, resulting in a certain distance in spatial matching. In this study, the upper limit of

692 distance is 0.5 degree. Figure 9 (d) shows the error of the distance between stations, where the
 693 degree is converted to the distance at WGS84 coordinates. The bias does not change significantly
 694 with increasing distance. The average bias is around 0, with the maximum positive mean bias
 695 (0.0322) at a distance of 2km and the maximum negative mean deviation (-0.0323) at 6km. The
 696 median is almost positive, except at 5km and 6km. The percentage falling within the EE envelopes
 697 is over 50%, with the maximum percentage (66%) at 3km and the minimum (62%) at 2km.



698

699 **Figure 9:** Box plots of AOD bias and the percentage falling within the EE envelopes (curves): (a)
 700 AERONET AOD levels, (b) elevation of AERONET sites, (c) elevation difference between
 701 meteorological stations and AERONET sites, (d) distance (km) between meteorological stations and
 702 AERONET sites. The black horizontal line represents the zero bias. For each box, the upper, lower,
 703 and middle horizontal lines, and whiskers represent the AOD bias 75th and 25th percentiles, median,
 704 and 1.5 times the interquartile difference, respectively. The black solid lines represent the EE
 705 envelopes ($\pm(0.05+0.15*AOD_{AERONET})$). No site with a difference of +0.3km (x-axis label without
 706 0.3) in (c).

707 3.4 Interannual variability and trend of visibility-derived AOD over global land

708 The multi-year average AOD from 1980 to 2021 over land is 0.177, as shown in Figure 10 (a). The
 709 average is 0.178 in Northern Hemisphere (NH, 4532 stations) and 0.174 in Southern Hemispheres
 710 (SH, 500 stations). Due to the influence of geography, atmospheric circulation, population, and
 711 emissions, the AOD varies in different latitudes. Figure 11 illustrates the multi-year average AOD
 712 in different latitude ranges from 1980 to 2021. The AOD value in the NH is higher than that over
 713 land, then higher than that in the SH. Within [-20, 20°N], the average AOD reaches its maximum
 714 (0.2225), and the maximum AOD in the NH is 0.239 in [0, 20°N]. The highest AOD in the SH is
 715 0.203 in in [-15, 0°N]. The average AOD rapidly decreases from -15°N to -35°N in the SH and from
 716 20°N to 50°N in the NH.

717 There are many regions of high AOD values occur in the NH, with the distribution of high

718 population density. Approximately 7/8 of the global population resides in the NH, with 50%
719 concentrated at 20°N-40°N (Kummu et al., 2016), indicating a significant impact of human activities
720 on aerosols. The highest AOD values are observed near 17°N, including the Sahara Desert, Arabian
721 Peninsula, and India, suggesting that in addition to anthropogenic sources, deserts also play a crucial
722 role in aerosol emissions. Lower AOD regions of the SH are from 25°S to 60°S, encompassing
723 Australia, southern Africa, and southern South America, indicating lower aerosol burdens in these
724 areas. Additionally, North America also exhibits low aerosol loading. Chin et al. (2014) analyzed
725 the AOD over land from 1980 to 2009 with the Goddard Chemistry Aerosol Radiation and Transport
726 model, which is similar to the visibility-derived AOD. The spatial distribution is consistent with the
727 satellite results (Remer et al., 2008; Hsu et al., 2012; Hsu et al., 2017; Tian et al., 2023). The AOD
728 and extinction coefficient retrieved from visibility show a similar distribution at global scale, with
729 a correlation coefficient of nearly 0.6 (Mahowald et al., 2007). Similar global (Husar et al., 2000;
730 Wang et al., 2009) and regional (Koelemeijer et al., 2006; Wu et al., 2014; Boers et al., 2015; Zhang
731 et al., 2017; Zhang et al., 2020) spatial distributions have been reported.

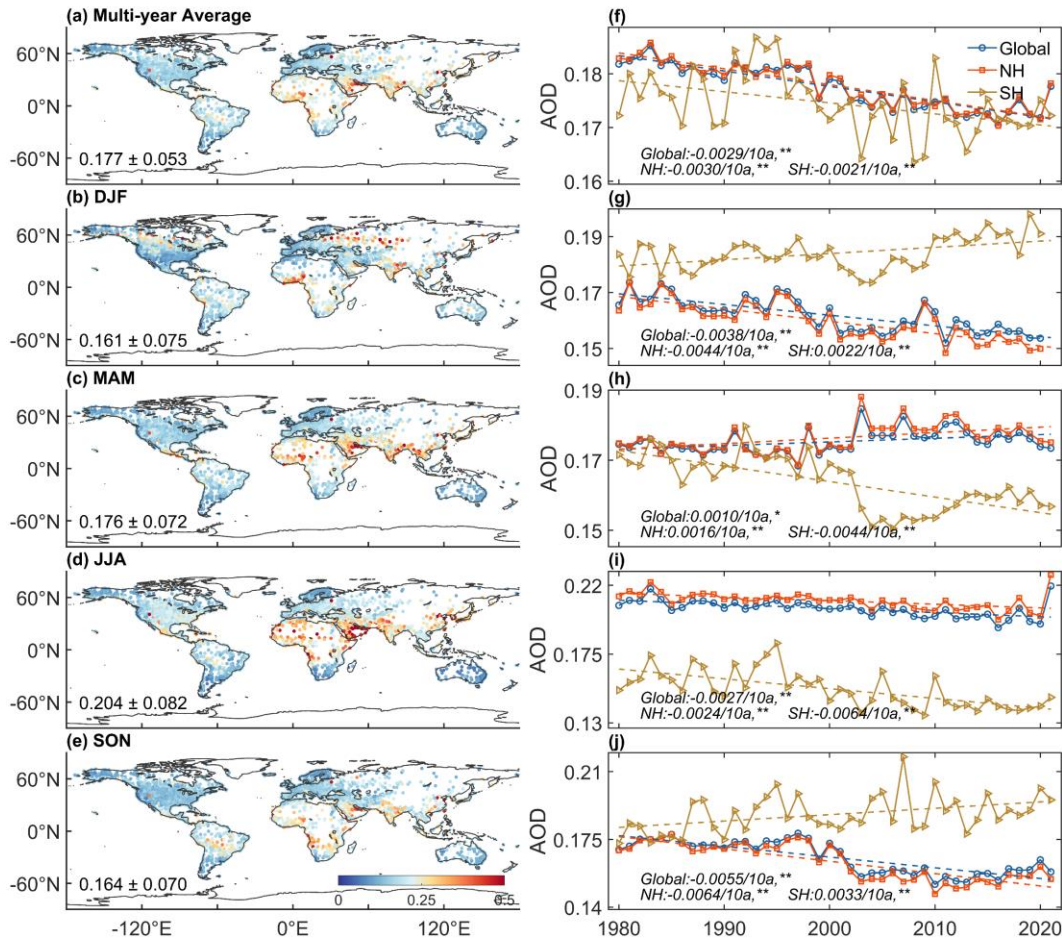
732 AOD loadings exhibit significant seasonal variations worldwide, particularly over land. In this study,
733 a year is divided into four parts: December-January-February (DJF), March-April-May (MAM),
734 June-July-August (JJA), and September-October-November (SON), corresponding to winter
735 (summer), spring (autumn), summer (winter), and autumn (spring) in the NH (SH), respectively.
736 Figure 10 (b-e) also depicts the spatial distribution of seasonal average AOD over land from 1980
737 to 2021. The global AOD in DJF, MAM, JJA, and SON is 0.162, 0.175, 0.205, and 0.1166,
738 respectively. The standard bias of AOD in JJA and DJF are greater than those in DJF and SON.
739 AOD exhibits seasonal changes, with the highest in JJA, followed by MAM, DJF, and SON.

740 In the NH, the AOD ranking is summer (0.210) > spring (0.176) > autumn (0.163) > winter (0.160).
741 In the SH, the AOD ranking from high to low in season is spring (0.188) > summer (0.184) > autumn
742 (0.164) > winter (0.152). The highest AOD is observed during JJA in the NH, while in the SH, the
743 peak occurs during SON. The high AOD value is highly associated with the growth of hygroscopic
744 particle and the photochemical reaction of aerosol precursors under higher relative humidity in Asia
745 (JJA) (Remer et al., 2008) and Europe such as Russia (JJA), and biomass burning in South America
746 (SON), Southern Africa (SON), and Indonesia (SON) (Ivanova et al., 2010; Krylov et al., 2014). On
747 the other hand, the lowest global AOD values are observed during winter, which may be attributed
748 to the atmospheric circulation systems (Li et al., 2016; Zhao et al., 2019).

749 The temporal variations in AOD have also been of great interest due to the significant relationship
750 between aerosols and climate change. Figure 10 (f) shows the trends of annual average AOD (**
751 represents passing the significance test, $p < 0.01$) over the global land, the SH and the NH during
752 1980-2021. The global land, NH, and SH trends demonstrate decreasing trends of AOD with values
753 of -0.0029/10a, -0.0030/10a, and -0.0021/10a, respectively, with all passing the significance test.
754 The declining trend is much greater in the NH than in the SH.

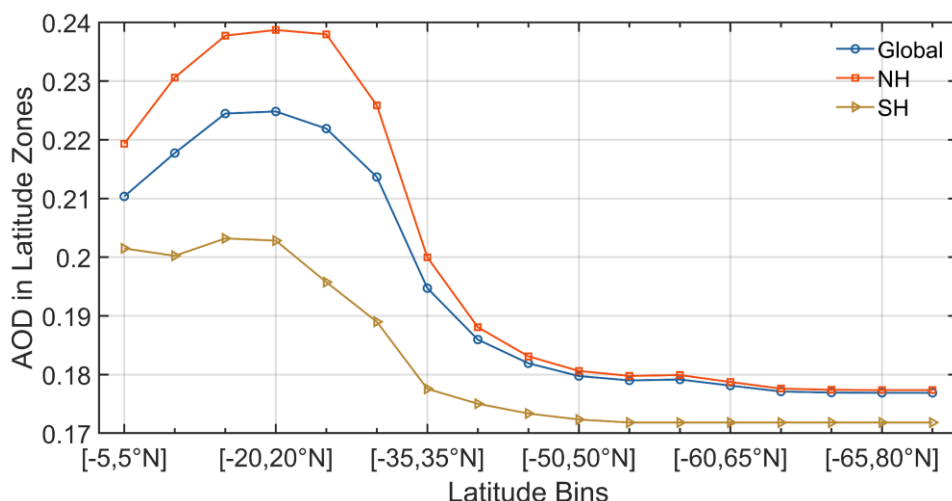
755 The seasonal trends of AOD during 1980-2021 at the global and hemispheric scales are shown in
756 Figure 10 (g-j). The trend over land is decreasing in DJF, JJA and SON, and increasing in MAM.
757 The largest declining trend is observed in SON (-0.0055/10a). In the NH, the trends are -0.0044/10a
758 (DJF), 0.0016/10a (MAM), -0.0024/10a (JJA), and -0.0064/10a (SON). In the SH, the trends are as
759 follows: 0.0022/10a (DJF), -0.0044/10a (MAM), -0.00064/10a (JJA), and 0.0033/10a (SON). The

760 largest declining trend is autumn in the NH and JJA in the SH. However, the trends are positive in
 761 MAM of the NH and DJF and SON of the SH.



762

763 **Figure 10:** The multi-year and average seasonal AOD and from 1980 to 2021. Global land (circle),
 764 northern hemisphere (NH) (triangle) and southern hemisphere (SH) (square) annual and seasonal
 765 AOD. The symbol, **, represents that the test passed at a significance level of 0.01. The symbol, *,
 766 represents that the test passed at a significance level of 0.05. DJF represents December and next
 767 January and February. MAM represents March, April, and May. JJA represents June, July, and
 768 August. SON represents September, October, and November.



769

770 **Figure 11:** The global land (blue), northern hemisphere's (red) and southern hemisphere's (yellow)
 771 multi-year average VIS_AOD from 1980 to 2021 in different latitude zones. The latitude range is
 772 from -65 to 85°N, with a bin of 5°.

773 3.5 Interannual variability and trend of visibility-derived AOD over regions

774 The distribution of AOD over global land exhibits significant spatial heterogeneity. Large variations
 775 in aerosol concentrations exist among different regions, leading to a non-uniform spatial distribution
 776 of AOD globally. Accurately assessing the long-term trends of aerosol loading is a key for
 777 quantifying aerosol climate change, and it is crucial for evaluating the effectiveness of
 778 measurements implemented to improve regional air quality and reduce anthropogenic aerosol
 779 emissions. Therefore, we select 12 representative regions to analyze the variability and trend of AOD,
 780 which are influenced by various aerosol sources (Wang et al., 2009; Hsu et al., 2012; Chin et al.,
 781 2014), such as desert, industry, anthropogenic emissions, and biomass burning emissions, which
 782 nearly cover the most land and are densely populated regions (Kummu et al., 2016). These
 783 representative regions are Eastern Europe, Western Europe, Western North America, Eastern North
 784 America, Central South America, Western Africa, Southern Africa, Australia, Southeast Asia,
 785 Northeast Asia, Eastern China, and India, as shown in Figure 1.

786 The multi-year average and seasonal average AOD (Figure 12), the trends of the annual average of
 787 monthly anomalies (Figure 13), and the seasonal trends (Figure 14) are analyzed in 12 regions from
 788 1980 to 2021.

789 The regions with a high aerosol level ($AOD > 0.2$) are in West Africa, Southeast and Northeast Asia,
 790 Eastern China, and India. The AOD values range from 0.15 to 0.2 in Eastern Europe, Western
 791 Europe, Eastern North America, Central South America, and South Africa. The AOD values are less
 792 than 0.15 in Western North America and Australia.

793 Europe is an industrial region with a low aerosol loading region, and the multi-year average AOD
 794 in Eastern Europe (0.181) is higher than that in Western Europe (0.1163) during 1980-2021. Eastern
 795 Europe shows a greater downward trend in AOD (-0.0067/10a) compared to Western Europe (-
 796 0.0026/10a). The highest AOD is observed in JJA, the dry period when solar irradiation and
 797 boundary layer height increase, with Eastern Europe at 0.201 and Western Europe at 0.162, which

798 could be due to increases in secondary aerosols, biomass burning, and dust transport from the Sahara
799 (Mehta et al., 2016). However, there are seasonal variations. In Eastern Europe, the seasonal AOD
800 ranking from high to low is JJA (0.201) > DJF (0.181) > MAM (0.175) > SON (0.161), while in
801 Western Europe, it is JJA (0.193) > MAM (0.162) > SON (0.160) > DJF (0.138). The differences
802 among seasons are larger in Western Europe. AOD in Eastern Europe shows declining trends
803 ($p < 0.01$) in all seasons, and the largest declining trend is in DJF (-0.0096/10a). In Western Europe,
804 the trend in DJF, JJA, and SON exhibit declining trends, while the trend in MAM shows a significant
805 increase trend (0.0019/10a). The trends in both Western and Eastern Europe are increasing in MAM
806 from 1995 to 2005 with Western Europe showing a greater increase. However, after 2005, the
807 decline rates accelerate in each season. Studies have shown the downward trend in Europe is
808 attributed to the reduction of biomass burning, anthropogenic aerosols, and aerosol precursors (such
809 as sulfur dioxide)(Wang et al., 2009; Chin et al., 2014; Mortier et al., 2020).

810 North America is also an industrial region with a low aerosol loading. The average AOD values in
811 Eastern and Western North America during 1980-2021 are 0.165 and 0.146, respectively, with the
812 Eastern region being higher than the Western region by 0.019. From 1980 to 2021, both Eastern (-
813 0.0027/10a) and Western North America (-0.0017/10a) show a downward trend. The AOD values
814 in DJF, MAM, JJA, and SON in Western North America are 0.141, 0.148, 0.163, and 0.130,
815 respectively, compared to 0.138, 0.156, 0.216, and 0.149 in Eastern North America. Specifically,
816 the trends of the Western and Eastern region are increasing during MAM and decreasing during
817 other seasons. In the Western region, the trend is increasing after 2005, while in the Eastern region,
818 there is no increasing trend. The increasing trend may be due to low rainfall and increased wildfire
819 activities (Yoon et al., 2014). The decrease in Eastern North America is related to the reduction of
820 sulfate and organic aerosols, as well as the decrease in anthropogenic emissions caused by
821 environmental regulations (Mehta et al., 2016).

822 Central South America is a relatively high aerosol loading region, sourced from biomass burning,
823 especially in SON (Remer et al., 2008; Mehta et al., 2016), with a multi-year average AOD of 0.198.
824 There is a downward trend (-0.0075/10a) from 1980 to 2021. The trend is slightly lower than the
825 trend (-0.0090/10a) from 1998 to 2010 (Hsu et al., 2012) and the trend is decreasing from 1980 to
826 2006 (Streets et al., 2009) and from 2001 to 2014 (Mehta et al., 2016). The AOD values in DJF
827 (0.207) and SON (0.228) are higher compared to the values in MAM (0.185) and JJA (0.171), and
828 the larger declining trends are observed in MAM (-0.0100/10a) and JJA (-0.0150/10a). The result
829 indicates that although AOD has decreased overall, the aerosol loading is still high, which is caused
830 by seasonal deforestation and biomass burning (Mehta et al., 2016).

831 Africa is a high aerosol loading region worldwide. In West Africa, the multi-year average AOD is
832 0.281 during 1980-2021, and the trend is decreasing (-0.0062/10a). The world's largest desert
833 (Sahara Desert) is in West Africa, with much dust aerosol discharged. The AOD values in JJA
834 (0.296), MAM (0.292), DJF (0.276) and SON (0.261) are above 0.26. The trends in DJF (-
835 0.0145/10a), MAM (-0.0015/10a), JJA (-0.0019/10a) and SON (-0.0078/10) are decreasing. For
836 South Africa, the multi-year average AOD is 0.182, lower than that of West Africa. The trend is
837 decreasing (-0.0016/10a). The results of AERONET observations and simulation also show a
838 decreasing trend (Chin et al., 2014). The AOD values range from 0.12 to 0.20 during 2000-2009,
839 dominated by fine particle matter from industrial pollution from biomass and fossil fuel combustion

840 (Hersey et al., 2015). The average AOD values in DJF, MAM, JJA, and SON are 0.207, 0.173, 0.135,
841 and 0.21, with trends of 0.0044/10a, -0.0089/10a, -0.0089/10a and 0.0063/10a, respectively.

842 Australia is a region with a low aerosol loading. The multi-year average AOD is 0.133 during 1980-
843 2021. The AOD ranges from 0.05 to 0.15 from AERONET during 2000-2021, and dust and biomass
844 burning are important contributors to the aerosol loading (Yang et al., 2021a). There is a downward
845 trend of AOD (-0.0028/10a), which may be related to a decrease in dust and biomass burning (Yoon
846 et al., 2016; Yang et al., 2021a). In addition, a research has shown that the forest area in Australia
847 has increased sharply since 2000 (Giglio et al., 2013), surpassing the forest fire area of the past 14
848 years. The seasonal average of AOD in MAM, JJA, SON, and DJF are 0.130, 0.107, 0.132, and
849 0.161. The AOD in JJA is the lowest in all seasons and in all regions. The trends in DJF and SON
850 are increasing, and the trends in MAM and JJA are decreasing. Ground-based observations and
851 satellite retrievals indicate that wildfires, biomass burning and sandstorms lead to high AOD in DJF
852 and SON. The low AOD of MAM and JJA is due to a decrease in the frequency of sandstorms and
853 wildfires and an increase in precipitation (Gras et al., 1999; Yang et al., 2021a; Yang et al., 2021b).

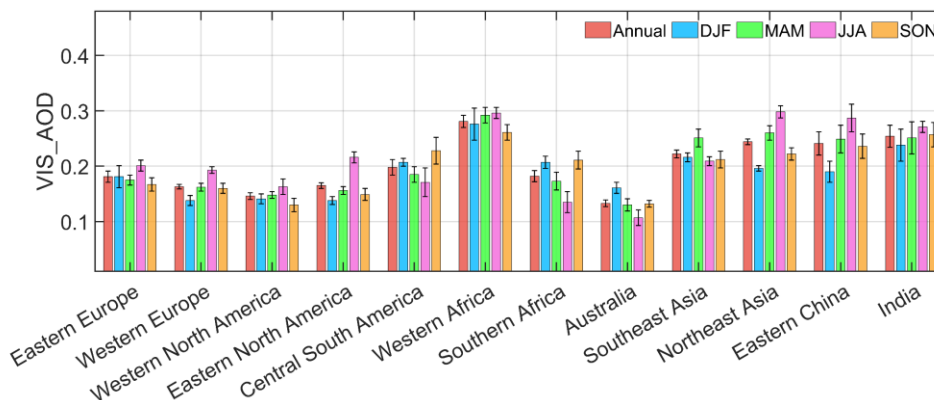
854 Asia is also a high aerosol loading area with various sources. In Southeast Asia, the multi-year
855 average AOD is 0.222 during 1980-2021 with a downward trend of AOD (0.0007/10a). It is also a
856 biomass-burning area. The seasonal average AOD ranking is MAM (0.251) > DJF (0.216) > SON
857 (0.212) > JJA (0.209). The trend in DJF (-0.0018/10a) is decreasing and the trends in MAM
858 (0.033/10a), JJA (0.0008/10a) and SON (0.0006/10a) are increasing. However, the trends are not
859 significant. Southeast Asia has no clear long-term trend in estimated AOD or ground-based
860 observations (Streets et al., 2009). In Northeast Asia, the multi-year average AOD is 0.244 during
861 1980-2021, with a trend of -0.0009/10a). The trend is increasing (0.0018/10a) during 1980-2014
862 and decreasing (-0.0213/10a) during 2014-2021. The seasonal AOD values are 0.196 in DJF, 0.260
863 in MAM, 0.287 in JJA and 0.236 in SON. The high aerosol level is related to dust aerosol and
864 aerosol transportation in East Asia. The trends in DJF (0.0016/10a), MAM (0.0062/10a) are
865 increasing, and the trends in JJA (-0.0043/10a) and SON (-0.0070/10a) are decreasing. In Eastern
866 China, the multi-year average AOD is 0.241, with an increasing trend (0.0130/10a). The trend is
867 0.0196/10a from 1980 to 2014 and -0.0572/10a from 2014 to 2021. The seasonal average AOD
868 ranking from high to low is JJA (0.287), MAM (0.249), SON (0.236) and DJF (0.216). The AOD
869 trends in DJF (0.0133/10a), MAM (0.0179/10a), JJA (0.0107/10a) and SON (0.0105/10a) are all
870 positive. The trend can be divided into three stages: 1980-2005, 2006-2013 and 2014-2021. In the
871 first stage, AOD values are increasing steadily. In the second stage, AOD values maintain a high
872 level. In the third stage, the AOD values experience a rapid decline, reaching the level in 1980s by
873 2021. The increasing trend of AOD before 2006 may be due to the significant increase in industrial
874 activity, and after 2013, the significant decrease is closely related to the implementation of air
875 quality-related laws and regulations, along with adjustments in the energy structure (Hu et al., 2018;
876 Cherian and Quaas, 2020).

877 India is a high aerosol loading area. The multi-year average AOD is 0.254, with a decreasing trend
878 (0.0119/10a) from 1980 to 2021. Dust and biomass burning has an influence on AOD level. There
879 are three stages: 1980-1997 (0.0050/10a), 1997-2005 (-0.0393/10a), 2005-2021 (0.0446/10a). The
880 seasonal average AOD values are 0.238 in DJF, 0.251 in MAM, 0.271 in JJA, and 0.257 in SON.
881 The largest AOD is in JJA. In winter and autumn, the aerosol level is affected by biomass burning,
882 and in spring and summer, it is also affected by dust, transported from the Sahara under during the

883 monsoon period (Remer et al., 2008). The trends in DJF (0.0186/10a), MAM (0.0143/10a), JJA
884 (0.0012/10a), and SON (0.0129/10a) are positive.

885 The above results have supplemented the long-term AOD variability and trend over land. The AOD
886 level at regional scale is significant differences from 1980 to 2021, which is significantly related to
887 the aerosol emission source type, transportation and the implementation of laws and regulations
888 about pollution control.

889

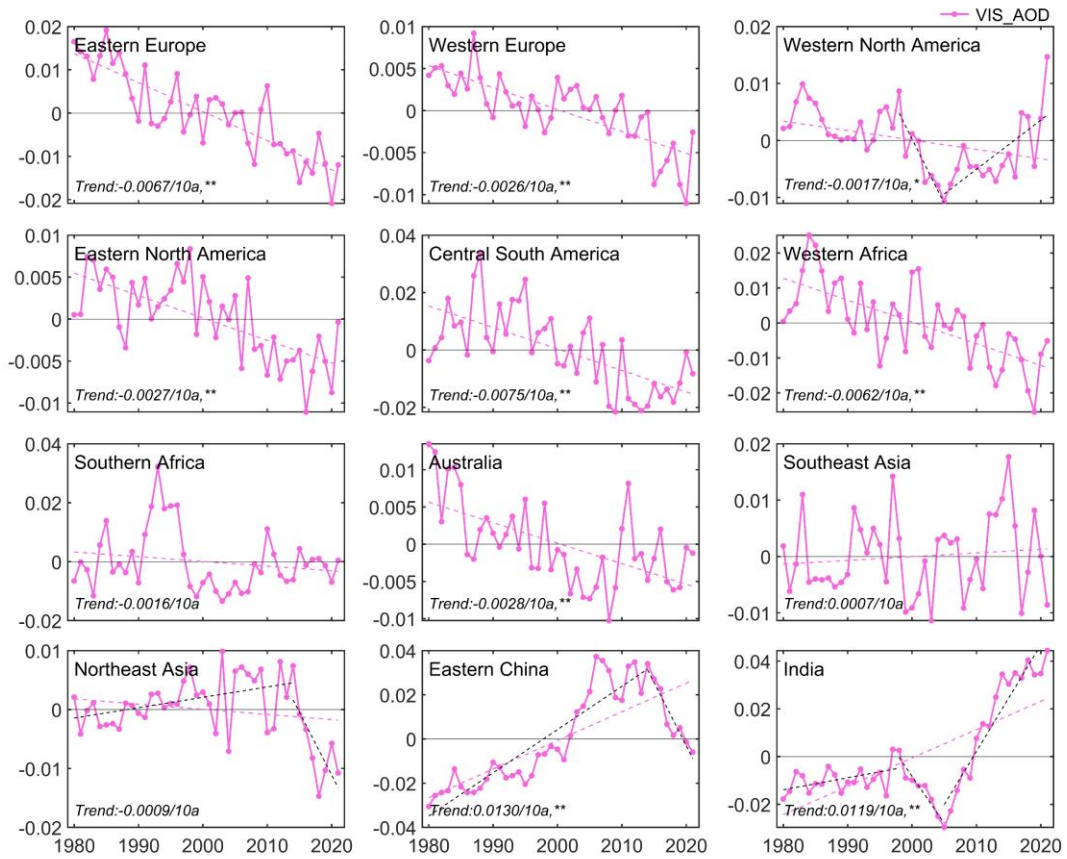


890

891 **Figure 12:** Annual and seasonal average AOD in 12 regions (Eastern Europe, Western Europe,
892 Western North America, Eastern North America, Central South America, Western Africa, Southern
893 Africa, Australia, Southeast Asia, Northeast Asia, Eastern China, and India) during 1980-2021.

894

895



896

897 **Figure 13:** Annual averages of monthly VIS_AOD anomaly VIS_AOD from 1980 to 2021 in 12
 898 regions (Eastern Europe, Western Europe, Western North America, Eastern North America, Central
 899 South America, Western Africa, Southern Africa, Australia, Southeast Asia, Northeast Asia, Eastern
 900 China, and India). The dotted line is the trend line.

901

902



903

904 **Figure 14:** Seasonal average VIS_AOD from 1980 to 2021 in 12 regions (Eastern Europe, Western
 905 Europe, Western North America, Eastern North America, Central South America, Western Africa,
 906 Southern Africa, Australia, Southeast Asia, Northeast Asia, Eastern China, and India). The dotted
 907 line is the trend line.

908 4 Data availability

909 We provide the daily visibility-derived AOD data at 5032 stations over global land, which is
 910 available at National Tibetan Plateau / Third Pole Environment Data Center,
 911 <https://doi.org/10.11888/Atmos.tpcdc.300822> (Hao et al., 2023). Due to a small number and sparse
 912 visibility stations prior to 1980, the global/regional analysis in this study is from 1980 to 2021. The
 913 following is a description to the AOD dataset.

914 The station-scale AOD files are in ‘Station_Daily_AOD_1959_2021.zip’. The station-scale AOD
 915 files can be directly opened by a text program (such as Notepad). The details station information is
 916 in the file of ‘0A0A-Station_Information.txt’. There are eight columns in each text file, separated
 917 by commas and the column names are Datetime, TEMP (°C), DEW (°C), RH (%), WS (m/s), SLP
 918 (hPa), DRYVIS (km), and VIS_AOD (550nm). The first column name is the date. The column name,
 919 ‘VIS_AOD (550nm)’, is the AOD at 550nm. The 2-7th column names are temperature (unit: °C),
 920 dew temperature (unit: °C), relative humidity (unit: %), wind speed (unit: m/s), sea level pressure
 921 (unit: hPa), and dry visibility (unit: km). The more details are in ‘0A0B-ReadMe.txt’.

922 5 Conclusions

923 In this study, we employ a machine learning method to derive daily AOD at 550nm from 1980 to
924 2021 at 5032 land stations worldwide, based on visibility, satellite retrieval, and related
925 meteorological variables. In the model, Aqua MODIS AOD (550nm) is set as the target and visibility
926 and related meteorological variables are set as the predictor. The performance and predictive ability
927 of the model are evaluated and validated against AERONET ground-based observations, Terra
928 MODIS AOD and MRRRA-2 AOD. We provide a long-term daily AOD (550nm) dataset at 5032
929 global land stations from 1980 to 2021. The dataset has complemented the shortcomings of AOD
930 data in terms of time scale and spatial coverage over land. Finally, the variability and trend of AOD
931 are analyzed at global and regional scales in the past 42 years. Several key findings have been given
932 in this study as follows.

933 **1. Modeling evaluation.** For all stations, the mean RMSE, MAE, and R of the model are 0.078,
934 0.044, and 0.75, respectively. The RMSE of 93% stations is less than 0.110, the MAE of 91% is less
935 than 0.060, and the R of 88% is greater than 0.70.

936 **2. Model validation.** For the daily scale, the R, RMSE and MAE of between VIS_AOD and Aqua
937 AOD is 0.799, 0.079 and 0.044, respectively. The percentage of sample point falling within the EE
938 envelopes is 84.12%. The R between VIS_AOD and Terra AOD is 0.542, with a RMSE of 0.125
939 and MAE of 0.078. The percentage falling within the EE envelopes is 64.76%. The R between
940 VIS_AOD and AERONET AOD is 0.546, with a RMSE of 0.186 and MAE of 0.099. The percentage
941 falling within the EE envelopes is 57.87%. For the monthly and annual scales, RMSE and MAE
942 show a significant decrease between VIS_AOD and Aqua, Terra, and AERONET AOD, and R and
943 percentages falling within EE show a significant increase. Compared to AERONET AOD and
944 MERRA-2 AOD prior to 2000, the model has consistent predictive ability.

945 **3. Error analysis.** As the AOD value increases, the average bias increases. When the pollution level
946 is low (AOD <0.1), the average bias is 0.015, with 83% of data within the EE envelopes. As
947 pollution level increases, the negative average bias becomes significant and the underestimation
948 increases. The elevation of AERONET's site also causes a bias. In low elevation (≤ 0.5 km), there
949 is a negative bias, with a percentage of 60%-64% falling within the EE envelopes. In high elevation
950 (0.5-1.2km), there is a positive bias, with a percentage of 50%-65% falling within the EE envelopes.
951 When the elevation difference is negative (the elevation of the meteorological station is lower than
952 that of the AERONET site), there is a significant positive bias. When the difference is positive, the
953 mean bias approaches 0 or is positive. The influence of distance between the meteorological station
954 and AERONET site on bias is not significant.

955 **4. Global land AOD.** The AOD values from 1980 to 2021 are 0.177 over land, 0.178 in the NH and
956 0.174 in the SH, with a trend of -0.0029/10a, 0.0030/10a and -0.0021/10a, respectively. The seasonal
957 AOD rankings are JJA (0.204) > MAM (0.176) > SON (0.164) > DJF (0.161) over global land, and
958 JJA (0.210) > MAM (0.176) > SON (0.163) > DJF (0.160) in the NH, SON (0.188) > DJF (0.184) >
959 MAM (0.14) > JJA (0.152) in the SH. The largest decreasing trends are in SON of the NH (-
960 0.0064/10a) and in JJA of the SH (-0.0064/10a). The increasing trends are in MAM of the NH and
961 in SJF and SON of the SH.

962 **5. Regional AOD.** The high aerosol loading (AOD > 0.2) regions are West Africa, Southeast and
963 Northeast Asia, Eastern China, and India, with a trend of -0.0062/10a, 0.0007/10a, -0.0009/10a,
964 0.0133/10a, and 0.0119/10a, respectively. However, the trends are decreasing in Eastern China (-

965 0.0572/10a) and Northeast Asia (-0.0213/10a) after 2014 and the larger increasing trend is found
966 after 2005 in India (0.0446/10a). The moderate aerosol loading (AOD between 0.15 and 0.2) regions
967 are Eastern Europe, Western Europe, Eastern North America, Central South America, and South
968 Africa, with a trend of -0.0067/10a, -0.0026/10a, -0.0027/10a, -0.0062/10a, and -0.0016/10a,
969 respectively. The low aerosol loading (AOD <0.15) regions are Western North America and
970 Australia, with a trend of -0.0017/10a and -0.0028/10a. However, the trends in Southern Africa,
971 Southeast Asia and Northeast Asia are not significant.

972 **Competing interests**

973 The contact author has declared that none of the authors has any competing interests.

974 **Acknowledgments**

975 This work is supported by the National Key Research & Development Program of China
976 (2022YFF0801302) and the National Natural Science Foundation of China (41930970). The hourly
977 visibility data are downloaded from <https://mesonet.agron.iastate.edu/ASOS>. The Aerosol Robotic
978 Network (AERONET) 15-minute AOD data are downloaded from <https://aeronet.gsfc.nasa.gov>.
979 The MODIS AOD data are downloaded from <https://ladsweb.modaps.eosdis.nasa.gov>.

980 **References**

- 981 Ackerman, A. S., Hobbs, P. V., and Toon, O. B.: A model for particle microphysics, turbulent mixing,
982 and radiative transfer in the stratocumulus-topped marine boundary layer and comparisons with
983 measurements, *J. Atmos. Sci.*, 52, 1204-1236, [https://doi.org/10.1175/1520-
984 0469\(1995\)052<1204:AMFPMT>2.0.CO;2](https://doi.org/10.1175/1520-0469(1995)052<1204:AMFPMT>2.0.CO;2), 1995.
- 985 Albrecht, B. A.: Aerosols, cloud microphysics, and fractional cloudiness, *Science*, 245, 1227-1230,
986 <https://doi.org/10.1126/science.245.4923.1227>, 1989.
- 987 Anderson, T. L., Charlson, R. J., Bellouin, N., Boucher, O., Chin, M., Christopher, S. A., Haywood, J.,
988 Kaufman, Y. J., Kinne, S., Ogren, J. A., Remer, L. A., Takemura, T., Tanre, D., Torres, O., Trepte, C. R.,
989 Wielicki, B. A., Winker, D. M., and Yu, H. B.: An "A-Train" strategy for quantifying direct climate
990 forcing by anthropogenic aerosols, *B. Am. Meteorol. Soc.*, 86, 1795+, [https://doi.org/10.1175/Bams-86-
991 12-1795](https://doi.org/10.1175/Bams-86-12-1795), 2005.
- 992 Andersson, S. M., Martinsson, B. G., Vernier, J.-P., Friberg, J., Brenninkmeijer, C. A., Hermann, M., Van
993 Velthoven, P. F., and Zahn, A.: Significant radiative impact of volcanic aerosol in the lowermost
994 stratosphere, *Nat. Commun.*, 6, 7692, <https://doi.org/10.1038/ncomms8692>, 2015.
- 995 Andrews, E., Sheridan, P. J., Ogren, J. A., Hageman, D., Jefferson, A., Wendell, J., Alástuey, A., Alados-
996 Arboledas, L., Bergin, M., and Ealo, M.: Overview of the NOAA/ESRL federated aerosol network, *B.*
997 *Am. Meteorol. Soc.*, 100, 123-135, <https://doi.org/10.1175/BAMS-D-17-0175.1>, 2019.
- 998 Bergstrom, R. W., Pilewskie, P., Russell, P. B., Redemann, J., Bond, T. C., Quinn, P. K., and Sierau, B.:
999 Spectral absorption properties of atmospheric aerosols, *Atmos. Chem. Phys.*, 7, 5937-5943,
1000 <https://doi.org/10.5194/acp-7-5937-2007>, 2007.
- 1001 Berk, R. A.: Classification and Regression Trees (CART), in: *Statistical Learning from a Regression*
1002 *Perspective*, Springer New York, New York, NY, 1-65, https://doi.org/10.1007/978-0-387-77501-2_3,

1003 2008.

1004 Bescond, A., Yon, J., Girasole, T., Jouen, C., Rozé, C., and Coppalle, A.: Numerical investigation of the
1005 possibility to determine the primary particle size of fractal aggregates by measuring light depolarization,
1006 *J. Quant. Spectrosc. Ra.*, 126, 130-139, <https://doi.org/10.1016/j.jqsrt.2012.10.011>, 2013.

1007 Boers, R., van Weele, M., van Meijgaard, E., Savenije, M., Siebesma, A. P., Bosveld, F., and Stammes,
1008 P.: Observations and projections of visibility and aerosol optical thickness (1956-2100) in the
1009 Netherlands: impacts of time-varying aerosol composition and hygroscopicity, *Environ. Res. Lett.*, 10,
1010 <https://doi.org/10.1088/1748-9326/10/1/015003>, 2015.

1011 Bokoye, A. I., Royer, A., O'Neil, N., Cliche, P., Fedosejevs, G., Teillet, P., and McArthur, L.:
1012 Characterization of atmospheric aerosols across Canada from a ground-based sunphotometer network:
1013 AEROCAN, *Atmos. Ocean*, 39, 429-456, <https://doi.org/10.1080/07055900.2001.9649687>, 2001.

1014 Bösenberg, J. and Matthias, V.: EARLINET: A European Aerosol Research Lidar Network to Establish
1015 an Aerosol Climatology, Max Planck Institut Fur Meteorologie, 2003.

1016 Bright, J. M. and Gueymard, C. A.: Climate-specific and global validation of MODIS Aqua and Terra
1017 aerosol optical depth at 452 AERONET stations, *Sol. Energy*, 183, 594-605,
1018 <https://doi.org/10.1016/j.solener.2019.03.043>, 2019.

1019 Browne, M. W.: Cross-validation methods, *J. Math. Psychol.*, 44, 108-132,
1020 <https://doi.org/10.1006/jmps.1999.1279>, 2000.

1021 Calvo, A. I., Alves, C., Castro, A., Pont, V., Vicente, A. M., and Fraile, R.: Research on aerosol sources
1022 and chemical composition: Past, current and emerging issues, *Atmos. Res.*, 120, 1-28,
1023 <https://doi.org/10.1016/j.atmosres.2012.09.021>, 2013.

1024 Chafe, Z. A., Brauer, M., Klimont, Z., Van Dingenen, R., Mehta, S., Rao, S., Riahi, K., Dentener, F., and
1025 Smith, K. R.: Household Cooking with Solid Fuels Contributes to Ambient PM_{2.5} Air Pollution and the
1026 Burden of Disease, *Environ. Health Persp.*, 122, 1314-1320, <https://doi.org/10.1289/ehp.1206340>, 2014.

1027 Chazette, P., David, C., Lefrère, J., Godin, S., Pelon, J., and Mégie, G.: Comparative lidar study of the
1028 optical, geometrical, and dynamical properties of stratospheric post-volcanic aerosols, following the
1029 eruptions of El Chichon and Mount Pinatubo, *J. Geophys. Res-Atmos.*, 100, 23195-23207,
1030 <https://doi.org/10.1029/95JD02268>, 1995.

1031 Che, H., Zhang, X., Chen, H., Damiri, B., Goloub, P., Li, Z., Zhang, X., Wei, Y., Zhou, H., Dong, F., Li,
1032 D., and Zhou, T.: Instrument calibration and aerosol optical depth validation of the China Aerosol Remote
1033 Sensing Network, *J. Geophys. Res-Atmos.*, 114, <https://doi.org/10.1029/2008jd011030>, 2009.

1034 Che, H., Xia, X., Zhu, J., Li, Z., Dubovik, O., Holben, B., Goloub, P., Chen, H., Estelles, V., Cuevas-
1035 Agullo, E., Blarel, L., Wang, H., Zhao, H., Zhang, X., Wang, Y., Sun, J., Tao, R., Zhang, X., and Shi, G.:
1036 Column aerosol optical properties and aerosol radiative forcing during a serious haze-fog month over
1037 North China Plain in 2013 based on ground-based sunphotometer measurements, *Atmos. Chem. Phys.*,
1038 14, 2125-2138, <https://doi.org/10.5194/acp-14-2125-2014>, 2014.

1039 Chen, A., Zhao, C., and Fan, T.: Spatio-temporal distribution of aerosol direct radiative forcing over mid-
1040 latitude regions in north hemisphere estimated from satellite observations, *Atmos. Res.*, 266, 105938,
1041 <https://doi.org/10.1016/j.atmosres.2021.105938>, 2022.

1042 Chen, D., Ou, T., Gong, L., Xu, C.-Y., Li, W., Ho, C.-H., and Qian, W.: Spatial Interpolation of Daily
1043 Precipitation in China: 1951-2005, *Adv. Atmos. Sci.*, 27, 1221-1232, <https://doi.org/10.1007/s00376-010-9151-y>, 2010.

1044 Cherian, R. and Quaas, J.: Trends in AOD, clouds, and cloud radiative effects in satellite data and CMIP5
1045 and CMIP6 model simulations over aerosol source regions, *Geophys. Res. Lett.*, 47, e2020GL087132,

1047 <https://doi.org/10.1029/2020GL087132>, 2020.

1048 Chin, M., Diehl, T., Tan, Q., Prospero, J., Kahn, R., Remer, L., Yu, H., Sayer, A., Bian, H., and
1049 Geogdzhayev, I.: Multi-decadal aerosol variations from 1980 to 2009: a perspective from observations
1050 and a global model, *Atmos. Chem. Phys.*, 14, 3657-3690, <https://doi.org/10.5194/acp-14-3657-2014>,
1051 2014.

1052 Chu, D., Kaufman, Y., Ichoku, C., Remer, L., Tanré, D., and Holben, B.: Validation of MODIS aerosol
1053 optical depth retrieval over land, *Geophys. Res. Lett.*, 29, MOD2-1-MOD2-4,
1054 <https://doi.org/10.1029/2001GL013205>, 2002.

1055 Chuang, P.-J. and Huang, P.-Y.: B-VAE: a new dataset balancing approach using batched Variational
1056 AutoEncoders to enhance network intrusion detection, *J. Supercomput.*, <https://doi.org/10.1007/s11227-023-05171-w>, 2023.

1058 Deuzé, J., Goloub, P., Herman, M., Marchand, A., Perry, G., Susana, S., and Tanré, D.: Estimate of the
1059 aerosol properties over the ocean with POLDER, *J. Geophys. Res-Atmos.*, 105, 15329-15346,
1060 <https://doi.org/10.1029/2000JD900148>, 2000.

1061 Dhanya, R., Paul, I. R., Akula, S. S., Sivakumar, M., and Nair, J. J.: F-test feature selection in Stacking
1062 ensemble model for breast cancer prediction, *Procedia. Comput. Sci.*, 171, 1561-1570,
1063 <https://doi.org/10.1016/j.procs.2020.04.167>, 2020.

1064 Diner, D. J., Beckert, J. C., Reilly, T. H., Bruegge, C. J., Conel, J. E., Kahn, R. A., Martonchik, J. V.,
1065 Ackerman, T. P., Davies, R., and Gerstl, S. A. W.: Multi-angle Imaging SpectroRadiometer (MISR)
1066 instrument description and experiment overview, *Ieee T. Geosci. Remote.*, 98, 1072-1087,
1067 <https://doi.org/10.1109/36.700992>, 1998.

1068 Dong, Y., Li, J., Yan, X., Li, C., Jiang, Z., Xiong, C., Chang, L., Zhang, L., Ying, T., and Zhang, Z.:
1069 Retrieval of aerosol single scattering albedo using joint satellite and surface visibility measurements,
1070 *Remote Sens. Environ.*, 294, 113654, <https://doi.org/10.1016/j.rse.2023.113654>, 2023.

1071 Dubovik, Oleg, Holben, Brent, Eck, Thomas, F., Smirnov, Alexander, and Kaufman: Variability of
1072 Absorption and Optical Properties of Key Aerosol Types Observed in Worldwide Locations, *J. Atmos.*
1073 *Sci.*, 59, 590-590, [https://doi.org/10.1175/1520-0469\(2002\)059<0590:VOAAOP>2.0.CO;2](https://doi.org/10.1175/1520-0469(2002)059<0590:VOAAOP>2.0.CO;2), 2002a.

1074 Dubovik, O., Smirnov, A., Holben, B. N., King, M. D., Kaufman, Y. J., Eck, T. F., and Slutsker, I.:
1075 Accuracy assessments of aerosol optical properties retrieved from Aerosol Robotic Network (AERONET)
1076 Sun and sky radiance measurements, *J. Geophys. Res-Atmos.*, 105, 9791-9806,
1077 <https://doi.org/10.1029/2000jd900040>, 2000.

1078 Dubovik, O., Holben, B., Eck, T. F., Smirnov, A., Kaufman, Y. J., King, M. D., Tanré, D., and Slutsker,
1079 I.: Variability of absorption and optical properties of key aerosol types observed in worldwide locations,
1080 *J. Atmos. Sci.*, 59, 590-608, [https://doi.org/10.1175/1520-0469\(2002\)059<0590:VOAAOP>2.0.CO;2](https://doi.org/10.1175/1520-0469(2002)059<0590:VOAAOP>2.0.CO;2),
1081 2002b.

1082 Eck, T. F., Holben, B. N., Reid, J. S., Sinyuk, A., Giles, D. M., Arola, A., Slutsker, I., Schafer, J. S.,
1083 Sorokin, M. G., and Smirnov, A.: The extreme forest fires in California/Oregon in 2020: Aerosol optical
1084 and physical properties and comparisons of aged versus fresh smoke, *Atmos. Environ.*, 305, 119798,
1085 <https://doi.org/10.1016/j.atmosenv.2023.119798>, 2023.

1086 Elterman, L.: Relationships between vertical attenuation and surface meteorological range, *Appl. Optics*,
1087 9, 1804-1810, <https://doi.org/10.1364/AO.9.001804>, 1970.

1088 Fan, H., Zhao, C., Yang, Y., and Yang, X.: Spatio-Temporal Variations of the
1089 PM_{2.5}/PM₁₀ Ratios and Its Application to Air Pollution Type Classification
1090 in China, *Front. Environ. Sci.*, 9, <https://doi.org/10.3389/fenvs.2021.692440>, 2021.

1091 Fernández, A., Garcia, S., Herrera, F., and Chawla, N. V.: SMOTE for learning from imbalanced data:
1092 progress and challenges, marking the 15-year anniversary, *J. Artif. Intell. Res.*, 61, 863-905,
1093 <https://doi.org/10.1613/jair.1.11192>, 2018.

1094 Forster, P., Ramaswamy, V., Artaxo, P., Berntsen, T., Betts, R., Fahey, D. W., Haywood, J., Lean, J., Lowe,
1095 D. C., and Myhre, G.: Changes in atmospheric constituents and in radiative forcing, *Climate Change*
1096 2007: The Physical Science Basis. Contribution of Working Group I to the 4th Assessment Report of the
1097 Intergovernmental Panel on Climate Change, 2007.

1098 Gelaro, R., McCarty, W., Suárez, M. J., Todling, R., Molod, A., Takacs, L., Randles, C. A., Darmenov,
1099 A., Bosilovich, M. G., Reichle, R., Wargan, K., Coy, L., Cullather, R., Draper, C., Akella, S., Buchard,
1100 V., Conaty, A., da Silva, A. M., Gu, W., Kim, G.-K., Koster, R., Lucchesi, R., Merkova, D., Nielsen, J.
1101 E., Partyka, G., Pawson, S., Putman, W., Rienecker, M., Schubert, S. D., Sienkiewicz, M., and Zhao, B.:
1102 The Modern-Era Retrospective Analysis for Research and Applications, Version 2 (MERRA-2), *J.*
1103 *Climate*, 30, 5419-5454, <https://doi.org/10.1175/JCLI-D-16-0758.1>, 2017.

1104 Giglio, L., Randerson, J. T., and Van Der Werf, G. R.: Analysis of daily, monthly, and annual burned area
1105 using the fourth-generation global fire emissions database (GFED4), *J. Geophys. Res-Biogeo.*, 118, 317-
1106 328, <https://doi.org/10.1002/jgrg.20042>, 2013.

1107 Giles, D. M., Sinyuk, A., Sorokin, M. G., Schafer, J. S., Smirnov, A., Slutsker, I., Eck, T. F., Holben, B.
1108 N., Lewis, J. R., Campbell, J. R., Welton, E. J., Korkin, S. V., and Lyapustin, A. I.: Advancements in the
1109 Aerosol Robotic Network (AERONET) Version 3 database – automated near-real-time quality control
1110 algorithm with improved cloud screening for Sun photometer aerosol optical depth (AOD) measurements,
1111 *Atmos. Meas. Tech.*, 12, 169-209, <https://doi.org/10.5194/amt-12-169-2019>, 2019.

1112 Goovaerts, P.: Geostatistical approaches for incorporating elevation into the spatial interpolation of
1113 rainfall, *Journal of Hydrology*, 228, 113-129, [https://doi.org/10.1016/s0022-1694\(00\)00144-x](https://doi.org/10.1016/s0022-1694(00)00144-x), 2000.

1114 Gras, J., Jensen, J., Okada, K., Ikegami, M., Zaizen, Y., and Makino, Y.: Some optical properties of smoke
1115 aerosol in Indonesia and tropical Australia, *Geophys. Res. Lett.*, 26, 1393-1396,
1116 <https://doi.org/10.1029/1999GL900275>, 1999.

1117 Guerrero-Rascado, J. L., Landulfo, E., Antuña, J. C., Barbosa, H. d. M. J., Barja, B., Bastidas, Á. E.,
1118 Bedoya, A. E., da Costa, R. F., Estevan, R., and Forno, R.: Latin American Lidar Network (LALINET)
1119 for aerosol research: Diagnosis on network instrumentation, *J. Atmos. Sol-Terr. Phys.*, 138, 112-120,
1120 <https://doi.org/10.1016/j.jastp.2016.01.001>, 2016.

1121 Guo, J., Zhang, J., Yang, K., Liao, H., Zhang, S., Huang, K., Lv, Y., Shao, J., Yu, T., and Tong, B.:
1122 Investigation of near-global daytime boundary layer height using high-resolution radiosondes: first
1123 results and comparison with ERA5, MERRA-2, JRA-55, and NCEP-2 reanalyses, *Atmos. Chem. Phys.*,
1124 21, 17079-17097, <https://doi.org/10.5194/acp-21-17079-2021>, 2021.

1125 Hao, H., Wang, K., and Wu, G.: Visibility-derived aerosol optical depth over global land (1980-2021),
1126 National Tibetan Plateau Data Center [dataset], <https://doi.org/10.11888/Atmos.tpdc.300822>, 2023.

1127 He, H., Bai, Y., Garcia, E. A., and Li, S.: ADASYN: Adaptive synthetic sampling approach for
1128 imbalanced learning, *IEEE World Congress on Computational Intelligence*, 1322-1328,
1129 <https://doi.org/10.1109/IJCNN.2008.4633969>, 2008.

1130 Hersbach, H., Bell, B., Berrisford, P., Hirahara, S., Horányi, A., Muñoz-Sabater, J., Nicolas, J., Peubey,
1131 C., Radu, R., and Schepers, D.: The ERA5 global reanalysis, *Q. J. Roy. Meteor. Soc.*, 146, 1999-2049,
1132 <https://doi.org/10.1002/qj.3803>, 2020.

1133 Hersey, S. P., Garland, R. M., Crosbie, E., Shingler, T., Sorooshian, A., Piketh, S., and Burger, R.: An
1134 overview of regional and local characteristics of aerosols in South Africa using satellite, ground, and

1135 modeling data, *Atmos. Chem. Phys.*, 15, 4259-4278, <https://doi.org/10.5194/acp-15-4259-2015>, 2015.

1136 Hirono, M. and Shibata, T.: Enormous increase of stratospheric aerosols over Fukuoka due to volcanic
1137 eruption of El Chichon in 1982, *Geophys. Res. Lett.*, 10, 152-154,
1138 <https://doi.org/10.1029/GL010i002p00152>, 1983.

1139 Hofmann, D., Barnes, J., O'Neill, M., Trudeau, M., and Neely, R.: Increase in background stratospheric
1140 aerosol observed with lidar at Mauna Loa Observatory and Boulder, Colorado, *Geophys. Res. Lett.*, 36,
1141 <https://doi.org/10.1029/2009GL039008>, 2009.

1142 Holben, B. N., Eck, T. F., Slutsker, I., Tanre, D., Buis, J. P., Setzer, A., Vermote, E., Reagan, J. A.,
1143 Kaufman, Y. J., Nakajima, T., Lavenu, F., Jankowiak, I., and Smirnov, A.: AERONET - A federated
1144 instrument network and data archive for aerosol characterization, *Remote Sens. Environ.*, 66, 1-16,
1145 [https://doi.org/10.1016/s0034-4257\(98\)00031-5](https://doi.org/10.1016/s0034-4257(98)00031-5), 1998.

1146 Hsu, N., Gautam, R., Sayer, A., Bettenhausen, C., Li, C., Jeong, M., Tsay, S.-C., and Holben, B.: Global
1147 and regional trends of aerosol optical depth over land and ocean using SeaWiFS measurements from
1148 1997 to 2010, *Atmos. Chem. Phys.*, 12, 8037-8053, <https://doi.org/10.5194/acp-12-8037-2012>, 2012.

1149 Hsu, N., Jeong, M. J., Bettenhausen, C., Sayer, A., Hansell, R., Seftor, C., Huang, J., and Tsay, S. C.:
1150 Enhanced Deep Blue aerosol retrieval algorithm: The second generation, *J. Geophys. Res-Atmos.*, 118,
1151 9296-9315, <https://doi.org/10.1002/jgrd.50712>, 2013.

1152 Hsu, N., Lee, J., Sayer, A., Carletta, N., Chen, S. H., Tucker, C., Holben, B., and Tsay, S. C.: Retrieving
1153 near-global aerosol loading over land and ocean from AVHRR, *J. Geophys. Res-Atmos.*, 122, 9968-
1154 9989, <https://doi.org/10.1002/2017JD026932>, 2017.

1155 Hsu, N. C., Tsay, S.-C., King, M. D., and Herman, J. R.: Deep blue retrievals of Asian aerosol properties
1156 during ACE-Asia, *Ieee T. Geosci. Remote.*, 44, 3180-3195, <https://doi.org/10.1109/tgrs.2006.879540>,
1157 2006.

1158 Hu, B., Zhang, X., Sun, R., and Zhu, X.: Retrieval of Horizontal Visibility Using MODIS Data: A Deep
1159 Learning Approach, *Atmosphere-Basel*, 10, <https://doi.org/10.3390/atmos10120740>, 2019.

1160 Hu, K., Kumar, K. R., Kang, N., Boiyo, R., and Wu, J.: Spatiotemporal characteristics of aerosols and
1161 their trends over mainland China with the recent Collection 6 MODIS and OMI satellite datasets, *Environ.*
1162 *Sci. Pollut. R.*, 25, 6909-6927, <https://doi.org/10.1007/s11356-017-0715-6>, 2018.

1163 Husar, R. B., Husar, J. D., and Martin, L.: Distribution of continental surface aerosol extinction based on
1164 visual range data, *Atmos. Environ.*, 34, 5067-5078, [https://doi.org/10.1016/s1352-2310\(00\)00324-1](https://doi.org/10.1016/s1352-2310(00)00324-1),
1165 2000.

1166 IPCC: Climate Change 2021: The Physical Science Basis, Cambridge University Press, New York, 2021.

1167 Ivanova, G., Ivanov, V., Kukavskaya, E., and Soja, A.: The frequency of forest fires in Scots pine stands
1168 of Tuva, Russia, *Environ. Res. Lett.*, 5, 015002, <https://doi.org/10.1088/1748-9326/5/1/015002>, 2010.

1169 Kang, Y., Kim, M., Kang, E., Cho, D., and Im, J.: Improved retrievals of aerosol optical depth and fine
1170 mode fraction from GOCI geostationary satellite data using machine learning over East Asia, *Isprs J.*
1171 *Photogramm.*, 183, 253-268, <https://doi.org/10.1016/j.isprsjprs.2021.11.016>, 2022.

1172 Kang, Y., Choi, H., Im, J., Park, S., Shin, M., Song, C.-K., and Kim, S.: Estimation of surface-level NO₂
1173 and O₃ concentrations using TROPOMI data and machine learning over East Asia, *Environ. Pollut.*, 288,
1174 117711, <https://doi.org/10.1016/j.envpol.2021.117711>, 2021.

1175 Karbowska, B. and Zembrzuski, W.: Fractionation and mobility of thallium in volcanic ashes after
1176 eruption of Eyjafjallajökull (2010) in Iceland, *B. Environ. Contam. Tox.*, 97, 37-43,
1177 <https://doi.org/10.1007/s00128-016-1831-6>, 2016.

1178 Kaufman, Y. J. and Boucher, O.: A satellite view of aerosols in the climate system, *Nature*, 419, 215-215,

1179 <https://doi.org/10.1038/nature01091>, 2002.

1180 Kim, D. H., Sohn, B. J., Nakajima, T., Takamura, T., Takemura, T., Choi, B. C., and Yoon, S. C.: Aerosol
1181 optical properties over east Asia determined from ground-based sky radiation measurements, *J. Geophys.*
1182 *Res-Atmos.*, 109, <https://doi.org/10.1029/2003jd003387>, 2004.

1183 Klett, J. D.: Lidar inversion with variable backscatter/extinction ratios, *Appl. Optics*, 24, 1638-1643,
1184 <https://doi.org/10.1364/AO.24.001638>, 1985.

1185 Koelemeijer, R., Homan, C., and Matthijsen, J.: Comparison of spatial and temporal variations of aerosol
1186 optical thickness and particulate matter over Europe, *Atmos. Environ.*, 40, 5304-5315,
1187 <https://doi.org/10.1016/j.atmosenv.2006.04.044>, 2006.

1188 Koschmieder, H.: Theorie der horizontalen Sichtweite, *Beitrage zur Physik der freien Atmosphere*, 12,
1189 33-55, 1924.

1190 Krylov, A., McCarty, J. L., Potapov, P., Loboda, T., Tyukavina, A., Turubanova, S., and Hansen, M. C.:
1191 Remote sensing estimates of stand-replacement fires in Russia, 2002–2011, *Environ. Res. Lett.*, 9,
1192 105007, <https://doi.org/10.1088/1748-9326/9/10/105007>, 2014.

1193 Kulmala, M., Vehkamäki, H., Petäjä, T., Dal Maso, M., Lauri, A., Kerminen, V. M., Birmili, W., and
1194 McMurry, P. H.: Formation and growth rates of ultrafine atmospheric particles: A review of observations,
1195 *J. Aerosol Sci.*, 35, 143-176, <https://doi.org/10.1016/j.jaerosci.2003.10.003>, 2004.

1196 Kumm, M., De Moel, H., Salvucci, G., Viviroli, D., Ward, P. J., and Varis, O.: Over the hills and further
1197 away from coast: global geospatial patterns of human and environment over the 20th–21st centuries,
1198 *Environ. Res. Lett.*, 11, 034010, <https://doi.org/10.1088/1748-9326/11/3/034010>, 2016.

1199 Lapen, D. R. and Hayhoe, H. N.: Spatial analysis of seasonal and annual temperature and precipitation
1200 normals in southern Ontario, Canada, *J. Great Lakes Res.*, 29, 529-544, [https://doi.org/10.1016/s0380-1330\(03\)70457-2](https://doi.org/10.1016/s0380-1330(03)70457-2), 2003.

1202 Lee, L. A., Reddington, C. L., and Carslaw, K. S.: On the relationship between aerosol model uncertainty
1203 and radiative forcing uncertainty, *P. Natl. A. Sci.*, 113, 5820-5827,
1204 <https://doi.org/10.1073/pnas.1507050113>, 2016.

1205 Levy, R., Remer, L., Kleidman, R., Mattoo, S., Ichoku, C., Kahn, R., and Eck, T.: Global evaluation of
1206 the Collection 5 MODIS dark-target aerosol products over land, *Atmos. Chem. Phys.*, 10, 10399-10420,
1207 <https://doi.org/10.5194/acp-10-10399-2010>, 2010.

1208 Levy, R. C., Remer, L. A., Mattoo, S., Vermote, E. F., and Kaufman, Y. J.: Second-generation operational
1209 algorithm: Retrieval of aerosol properties over land from inversion of Moderate Resolution Imaging
1210 Spectroradiometer spectral reflectance, *J. Geophys. Res-Atmos.*, 112,
1211 <https://doi.org/10.1029/2006JD007811>, 2007.

1212 Levy, R. C., Mattoo, S., Munchak, L. A., Remer, L. A., Sayer, A. M., Patadia, F., and Hsu, N. C.: The
1213 Collection 6 MODIS aerosol products over land and ocean, *Atmos. Meas. Tech.*, 6, 2989-3034,
1214 <https://doi.org/10.5194/amt-6-2989-2013>, 2013.

1215 Levy, R. C., Mattoo, S., Sawyer, V., Shi, Y., Colarco, P. R., Lyapustin, A. I., Wang, Y., and Remer, L. A.:
1216 Exploring systematic offsets between aerosol products from the two MODIS sensors, *Atmos. Meas. Tech.*,
1217 11, 4073-4092, <https://doi.org/10.5194/amt-11-4073-2018>, 2018.

1218 Li, J., Garshick, E., Hart, J. E., Li, L., Shi, L., Al-Hemoud, A., Huang, S., and Koutrakis, P.: Estimation
1219 of ambient PM_{2.5} in Iraq and Kuwait from 2001 to 2018 using machine learning and remote sensing,
1220 *Environ. Int.*, 151, <https://doi.org/10.1016/j.envint.2021.106445>, 2021.

1221 Li, J., Carlson, B. E., Yung, Y. L., Lv, D., Hansen, J., Penner, J. E., Liao, H., Ramaswamy, V., Kahn, R.
1222 A., Zhang, P., Dubovik, O., Ding, A., Lacis, A. A., Zhang, L., and Dong, Y.: Scattering and absorbing

1223 aerosols in the climate system, *Nat. Rev. Earth. Environ.*, 3, 363-379, [https://doi.org/10.1038/s43017-](https://doi.org/10.1038/s43017-022-00296-7)
1224 [022-00296-7](https://doi.org/10.1038/s43017-022-00296-7), 2022.

1225 Li, S., Chen, L., Huang, G., Lin, J., Yan, Y., Ni, R., Huo, Y., Wang, J., Liu, M., and Weng, H.: Retrieval
1226 of surface PM_{2.5} mass concentrations over North China using visibility measurements and GEOS-Chem
1227 simulations, *Atmos. Environ.*, 222, 117121, <https://doi.org/10.1016/j.atmosenv.2019.117121>, 2020.

1228 Li, Z., Lau, W. M., Ramanathan, V., Wu, G., Ding, Y., Manoj, M., Liu, J., Qian, Y., Li, J., and Zhou, T.:
1229 Aerosol and monsoon climate interactions over Asia, *Rev. Geophys.*, 54, 866-929,
1230 <https://doi.org/10.1002/2015RG000500>, 2016.

1231 Liao, H., Chang, W., and Yang, Y.: Climatic Effects of Air Pollutants over China: A Review, *Adv. Atmos.*
1232 *Sci.*, 32, 115-139, <https://doi.org/10.1007/s00376-014-0013-x>, 2015.

1233 Lin, J. T., van Donkelaar, A., Xin, J. Y., Che, H. Z., and Wang, Y. S.: Clear-sky aerosol optical depth over
1234 East China estimated from visibility measurements and chemical transport modeling, *Atmos. Environ.*,
1235 95, 258-267, <https://doi.org/10.1016/j.atmosenv.2014.06.044>, 2014.

1236 Liu, B., Ma, X., Ma, Y., Li, H., Jin, S., Fan, R., and Gong, W.: The relationship between atmospheric
1237 boundary layer and temperature inversion layer and their aerosol capture capabilities, *Atmos. Res.*, 271,
1238 <https://doi.org/10.1016/j.atmosres.2022.106121>, 2022.

1239 Mahowald, N. M., Ballantine, J. A., Feddema, J., and Ramankutty, N.: Global trends in visibility:
1240 implications for dust sources, *Atmos. Chem. Phys.*, 7, 3309-3339, [https://doi.org/10.5194/acp-7-3309-](https://doi.org/10.5194/acp-7-3309-2007)
1241 [2007](https://doi.org/10.5194/acp-7-3309-2007), 2007.

1242 McNeill, V. F.: Atmospheric Aerosols: Clouds, Chemistry, and Climate, in: *Annu. Rev. Chem. Biomol.*,
1243 edited by: Prausnitz, J. M., *Annual Review of Chemical and Biomolecular Engineering*, 427-444,
1244 <https://doi.org/10.1146/annurev-chembioeng-060816-101538>, 2017.

1245 Mehta, M., Singh, R., Singh, A., and Singh, N.: Recent global aerosol optical depth variations and
1246 trends—A comparative study using MODIS and MISR level 3 datasets, *Remote Sens. Environ.*, 181,
1247 137-150, <https://doi.org/10.1016/j.rse.2016.04.004>, 2016.

1248 Mitra, R., Bajpai, A., and Biswas, K.: ADASYN-assisted machine learning for phase prediction of high
1249 entropy carbides, *Comp. Mater. Sci.*, 223, <https://doi.org/10.1016/j.commatsci.2023.112142>, 2023.

1250 Mortier, A., Gliß, J., Schulz, M., Aas, W., Andrews, E., Bian, H., Chin, M., Ginoux, P., Hand, J., and
1251 Holben, B.: Evaluation of climate model aerosol trends with ground-based observations over the last 2
1252 decades—an AeroCom and CMIP6 analysis, *Atmos. Chem. Phys.*, 20, 13355-13378,
1253 <https://doi.org/10.5194/acp-20-13355-2020>, 2020.

1254 Mukkavilli, S., Prasad, A., Taylor, R., Huang, J., Mitchell, R., Troccoli, A., and Kay, M.: Assessment of
1255 atmospheric aerosols from two reanalysis products over Australia, *Atmos. Res.*, 215, 149-164,
1256 <https://doi.org/10.1016/j.atmosres.2018.08.026>, 2019.

1257 Nagaraja Rao, C., Stowe, L., and McClain, E.: Remote sensing of aerosols over the oceans using AVHRR
1258 data Theory, practice and applications, *Int. J. Remote Sens.*, 10, 743-749,
1259 <https://doi.org/10.1080/01431168908903915>, 1989.

1260 Nakajima, T., Campanelli, M., Che, H., Estellés, V., Irie, H., Kim, S.-W., Kim, J., Liu, D., Nishizawa, T.,
1261 and Pandithurai, G.: An overview of and issues with sky radiometer technology and SKYNET, *Atmos.*
1262 *Meas. Tech.*, 13, 4195-4218, <https://doi.org/10.5194/amt-13-4195-2020>, 2020.

1263 NOAA, DOD, FAA, and USN: Automated Surface Observing System (ASOS) User's Guide, 1998.

1264 O'Reilly, J. E., Maritorena, S., Mitchell, B. G., Siegel, D. A., Carder, K. L., Garver, S. A., Kahru, M., and
1265 McClain, C.: Ocean color chlorophyll algorithms for SeaWiFS, *J. Geophys. Res.*, 103, 24937-24953,
1266 <https://doi.org/10.1029/98jc02160>, 1998.

1267 Pebesma, E. J.: Multivariable geostatistics in S: the gstat package, *Comput. Geosci.*, 30, 683-691,
1268 <https://doi.org/10.1016/j.cageo.2004.03.012>, 2004.

1269 Qiu, J. and Lin, Y.: A parameterization model of aerosol optical depths in China, *Acta. Meteorol. Sin.*,
1270 59, 368-372, <https://doi.org/10.11676/qxxb2001.039>, 2001.

1271 Ramanathan, V., Crutzen, P. J., Kiehl, J., and Rosenfeld, D.: Aerosols, climate, and the hydrological cycle,
1272 *Science*, 294, 2119-2124, <https://doi.org/10.1126/science.1064034>, 2001.

1273 Remer, L. A., Kleidman, R. G., Levy, R. C., Kaufman, Y. J., Tanre, D., Mattoo, S., Martins, J. V., Ichoku,
1274 C., Koren, I., Yu, H., and Holben, B. N.: Global aerosol climatology from the MODIS satellite sensors,
1275 *J. Geophys. Res-Atmos.*, 113, <https://doi.org/10.1029/2007jd009661>, 2008.

1276 Remer, L. A., Kaufman, Y. J., Tanre, D., Mattoo, S., Chu, D. A., Martins, J. V., Li, R. R., Ichoku, C.,
1277 Levy, R. C., Kleidman, R. G., Eck, T. F., Vermote, E., and Holben, B. N.: The MODIS aerosol algorithm,
1278 products, and validation, *J. Atmos. Sci.*, 62, 947-973, <https://doi.org/10.1175/jas3385.1>, 2005.

1279 Salomonson, V. V., Barnes, W. L., Maymon, P. W., Montgomery, H. E., and Ostrow, H.: MODIS:
1280 advanced facility instrument for studies of the Earth as a system, *Ieee T. Geosci. Remote.*, 27, 145-153,
1281 <https://doi.org/10.1109/36.20292>, 1987.

1282 Sawamura, P., Vernier, J. P., Barnes, J. E., Berkoff, T. A., Welton, E. J., Alados-Arboledas, L., Navas-
1283 Guzmán, F., Pappalardo, G., Mona, L., and Madonna, F.: Stratospheric AOD after the 2011 eruption of
1284 Nabro volcano measured by lidars over the Northern Hemisphere, *Environ. Res. Lett.*, 7, 34013-
1285 34021(34019), <https://doi.org/10.1088/1748-9326/7/3/034013>, 2012.

1286 Schutgens, N., Tsyro, S., Gryspeerdt, E., Goto, D., Weigum, N., Schulz, M., and Stier, P.: On the spatio-
1287 temporal representativeness of observations, *Atmos. Chem. Phys.*, 17, 9761-9780,
1288 <https://doi.org/10.5194/acp-17-9761-2017>, 2017.

1289 Singh, A., Mahata, K. S., Rupakheti, M., Junkermann, W., Panday, A. K., and Lawrence, M. G.: An
1290 overview of airborne measurement in Nepal—Part 1: Vertical profile of aerosol size, number, spectral
1291 absorption, and meteorology, *Atmos. Chem. Phys.*, 19, 245-258, [https://doi.org/10.5194/acp-19-245-](https://doi.org/10.5194/acp-19-245-2019)
1292 [2019](https://doi.org/10.5194/acp-19-245-2019), 2019.

1293 Smirnov, A., Holben, B., Slutsker, I., Giles, D., McClain, C., Eck, T., Sakerin, S., Macke, A., Croot, P.,
1294 and Zibordi, G.: Maritime aerosol network as a component of aerosol robotic network, *J. Geophys. Res-*
1295 *Atmos.*, 114, <https://doi.org/10.1029/2008JD011257>, 2009.

1296 Streets, D. G., Yan, F., Chin, M., Diehl, T., Mahowald, N., Schultz, M., Wild, M., Wu, Y., and Yu, C.:
1297 Anthropogenic and natural contributions to regional trends in aerosol optical depth, 1980–2006, *J.*
1298 *Geophys. Res-Atmos.*, 114, <https://doi.org/10.1029/2008JD011624>, 2009.

1299 Sun, E., Xu, X., Che, H., Tang, Z., Gui, K., An, L., Lu, C., and Shi, G.: Variation in MERRA-2 aerosol
1300 optical depth and absorption aerosol optical depth over China from 1980 to 2017, *J. Atmos. Sol-Terr.*
1301 *Phy.*, 186, 8-19, <https://doi.org/10.1016/j.jastp.2019.01.019>, 2019.

1302 Sun, Y. and Zhao, C.: Influence of Saharan dust on the large-scale meteorological environment for
1303 development of tropical cyclone over North Atlantic Ocean Basin, *J. Geophys. Res-Atmos.*, 125,
1304 e2020JD033454, <https://doi.org/10.1029/2020JD033454>, 2020.

1305 Teixeira, A.: Classification and regression tree, *Rev. Mal. Respir.*, 21, 1174-1176,
1306 [https://doi.org/10.1016/S0761-8425\(04\)71596-X](https://doi.org/10.1016/S0761-8425(04)71596-X), 2004.

1307 Tian, X., Tang, C., Wu, X., Yang, J., Zhao, F., and Liu, D.: The global spatial-temporal distribution and
1308 EOF analysis of AOD based on MODIS data during 2003-2021, *Atmos. Environ.*, 302,
1309 <https://doi.org/10.1016/j.atmosenv.2023.119722>, 2023.

1310 Tupper, A., Oswalt, J. S., and Rosenfeld, D.: Satellite and radar analysis of the volcanic-cumulonimbi at

1311 Mount Pinatubo, Philippines, 1991, *J. Geophys. Res-Atmos.*, 110,
1312 <https://doi.org/10.1029/2004JD005499>, 2005.

1313 van der Veer, G., Voerkelius, S., Lorentz, G., Heiss, G., and Hoogewerff, J. A.: Spatial interpolation of
1314 the deuterium and oxygen-18 composition of global precipitation using temperature as ancillary variable,
1315 *Journal of Geochemical Exploration*, 101, 175-184, <https://doi.org/10.1016/j.gexplo.2008.06.008>, 2009.

1316 Vernier, J. P., Thomason, L. W., Pommereau, J. P., Bourassa, A., Pelon, J., Garnier, A., Hauchecorne, A.,
1317 Blanot, L., Trepte, C., and Degenstein, D.: Major influence of tropical volcanic eruptions on the
1318 stratospheric aerosol layer during the last decade, *Geophys. Res. Lett.*, 38,
1319 <https://doi.org/10.1029/2011GL047563>, 2011.

1320 Wang, K., Dickinson, R. E., and Liang, S.: Clear Sky Visibility Has Decreased over Land Globally from
1321 1973 to 2007, *Science*, 323, 1468-1470, <https://doi.org/10.1126/science.1167549>, 2009.

1322 Wang, K. C., Dickinson, R. E., Su, L., and Trenberth, K. E.: Contrasting trends of mass and optical
1323 properties of aerosols over the Northern Hemisphere from 1992 to 2011, *Atmos. Chem. Phys.*, 12, 9387-
1324 9398, <https://doi.org/10.5194/acp-12-9387-2012>, 2012.

1325 Wei, J., Li, Z., Peng, Y., and Sun, L.: MODIS Collection 6.1 aerosol optical depth products over land and
1326 ocean: validation and comparison, *Atmos. Environ.*, 201, 428-440,
1327 <https://doi.org/10.1016/j.atmosenv.2018.12.004>, 2019.

1328 Wei, J., Li, Z., Sun, L., Peng, Y., Liu, L., He, L., Qin, W., and Cribb, M.: MODIS Collection 6.1 3 km
1329 resolution aerosol optical depth product: Global evaluation and uncertainty analysis, *Atmos. Environ.*,
1330 240, 117768, <https://doi.org/10.1016/j.atmosenv.2020.117768>, 2020.

1331 Welton, E. J., Campbell, J. R., Berkoff, T. A., Spinhirne, J. D., and Starr, D. O.: The micro-pulse lidar
1332 network (MPLNET), *Frontiers in Optics*, <https://doi.org/10.1364/fio.2003.mk2>, 2002.

1333 Winker, D. M., Tackett, J. L., Getzewich, B. J., Liu, Z., Vaughan, M. A., and Rogers, R. R.: The global
1334 3-D distribution of tropospheric aerosols as characterized by CALIOP, *Atmos. Chem. Phys.*, 13, 3345-
1335 3361, <https://doi.org/10.5194/acp-13-3345-2013>, 2013.

1336 Winker, D. M., Vaughan, M. A., Omar, A., Hu, Y., Powell, K. A., Liu, Z., Hunt, W. H., and Young, S. A.:
1337 Overview of the CALIPSO Mission and CALIOP Data Processing Algorithms, *J. Atmos. Ocean. Tech.*,
1338 26, 2310-2323, <https://doi.org/10.1175/2009jtecha1281.1>, 2009.

1339 Wu, J., Luo, J., Zhang, L., Xia, L., Zhao, D., and Tang, J.: Improvement of aerosol optical depth retrieval
1340 using visibility data in China during the past 50years, *J. Geophys. Res-Atmos.*, 119, 13370-13387,
1341 <https://doi.org/10.1002/2014jd021550>, 2014.

1342 Xia, X., Che, H., Zhu, J., Chen, H., Cong, Z., Deng, X., Fan, X., Fu, Y., Goloub, P., and Jiang, H.: Ground-
1343 based remote sensing of aerosol climatology in China: Aerosol optical properties, direct radiative effect
1344 and its parameterization, *Atmos. Environ.*, 124, 243-251,
1345 <https://doi.org/10.1016/j.atmosenv.2015.05.071>, 2016.

1346 Yang, X., Zhao, C., Yang, Y., and Fan, H.: Long-term multi-source data analysis about the characteristics
1347 of aerosol optical properties and types over Australia, *Atmos. Chem. Phys.*, 21, 3803-3825,
1348 <https://doi.org/10.5194/acp-21-3803-2021>, 2021a.

1349 Yang, X., Zhao, C., Yang, Y., Yan, X., and Fan, H.: Statistical aerosol properties associated with fire
1350 events from 2002 to 2019 and a case analysis in 2019 over Australia, *Atmos. Chem. Phys.*, 21, 3833-
1351 3853, <https://doi.org/10.5194/acp-21-3833-2021>, 2021b.

1352 Yang, X., Wang, Y., Zhao, C., Fan, H., Yang, Y., Chi, Y., Shen, L., and Yan, X.: Health risk and disease
1353 burden attributable to long-term global fine-mode particles, *Chemosphere*, 287,
1354 <https://doi.org/10.1016/j.chemosphere.2021.132435>, 2022.

1355 Yang, Y., Ge, B., Chen, X., Yang, W., Wang, Z., Chen, H., Xu, D., Wang, J., Tan, Q., and Wang, Z.:
1356 Impact of water vapor content on visibility: Fog-haze conversion and its implications to pollution control,
1357 Atmos. Res., 256, <https://doi.org/10.1016/j.atmosres.2021.105565>, 2021c.

1358 Yoon, J., Burrows, J., Vountas, M. v., von Hoyningen-Huene, W., Chang, D., Richter, A., and Hilboll, A.:
1359 Changes in atmospheric aerosol loading retrieved from space-based measurements during the past decade,
1360 Atmos. Chem. Phys., 14, 6881-6902, <https://doi.org/10.5194/acp-14-6881-2014>, 2014.

1361 Yoon, J., Pozzer, A., Chang, D. Y., Lelieveld, J., Kim, J., Kim, M., Lee, Y., Koo, J.-H., Lee, J., and Moon,
1362 K.: Trend estimates of AERONET-observed and model-simulated AOTs between 1993 and 2013, Atmos.
1363 Environ., 125, 33-47, <https://doi.org/10.1016/j.atmosenv.2015.10.058>, 2016.

1364 Zhang, S., Wu, J., Fan, W., Yang, Q., and Zhao, D.: Review of aerosol optical depth retrieval using
1365 visibility data, Earth-Sci. Rev., 200, 102986, <https://doi.org/10.1016/j.earscirev.2019.102986>, 2020.

1366 Zhang, Z., Wu, W., Wei, J., Song, Y., Yan, X., Zhu, L., and Wang, Q.: Aerosol optical depth retrieval from
1367 visibility in China during 1973-2014, Atmos. Environ., 171, 38-48,
1368 <https://doi.org/10.1016/j.atmosenv.2017.09.004>, 2017.

1369 Zhao, A. D., Stevenson, D. S., and Bollasina, M. A.: The role of anthropogenic aerosols in future
1370 precipitation extremes over the Asian Monsoon Region, Clim. Dynam., 52, 6257-6278,
1371 <https://doi.org/10.1007/s00382-018-4514-7>, 2019.

1372